A non-genetic model of vascular shunts informs on the cellular mechanisms of formation and resolution of arteriovenous malformations

Marie Ouarné[1]*[†‡], Andreia Pena[1,2‡], Daniela Ramalho[1,2‡], Nadine V. Conchinha[1],
Tiago Costa[1], Romain Enjalbert[3], Ana M. Figueiredo[1], Marta Pimentel Saraiva[1],
Yulia Carvalho[1], Miguel O. Bernabeu[3,4], Lenka Henao Misikova[1,2], S. Paul Oh[5],
and Cláudio A. Franco [1,2]*

[1]Instituto de Medicina Molecular João Lobo Antunes, Faculdade de Medicina, Universidade de Lisboa, Lisbon 1649-028, Portugal; [2]Católica Biomedical Research Centre, Universidade Católica Portuguesa, Católica Medical School, Lisbon 1649-023, Portugal; [3]Centre for Medical Informatics, Usher Institute, The University of Edinburgh, Edinburgh EH16 4UX, UK; [4]The Bayes Centre, The University of Edinburgh, Edinburgh EH8 9BT, UK; and [5]Barrow Aneurysm & AVM Research Center, Department of Translational Neuroscience, Barrow Neurological Institute, Phoenix, AZ 85013, USA

Aims	Arteriovenous malformations (AVMs), a disorder characterized by direct shunts between arteries and veins, are associated with genetic mutations. However, the mechanisms leading to AV shunt formation and how shunts can be reverted are poorly understood.
Methods and results	Here, we report that oxygen-induced retinopathy (OIR) protocol leads to the consistent and stereotypical formation of AV shunts in non-genetically altered mice. OIR-induced AV shunts show all the canonical markers of AVMs. Genetic and pharmacological interventions demonstrated that changes in the volume of venous endothelial cells (EC)—hypertrophic venous cells—are the initiating step promoting AV shunt formation, whilst EC proliferation or migration played minor roles. Inhibition of the mTOR pathway prevents pathological increases in EC volume and significantly reduces the formation of AV shunts. Importantly, we demonstrate that ALK1 signalling cell-autonomously regulates EC volume in pro-angiogenic conditions, establishing a link with hereditary haemorrhagic telangiectasia-related AVMs. Finally, we demonstrate that a combination of EC volume control and EC migration is associated with the regression of AV shunts.
Conclusion	Our findings highlight that an increase in the EC volume is the key mechanism driving the initial stages of AV shunt formation, leading to asymmetric capillary diameters. Based on our results, we propose a coherent and unifying timeline leading to the fast conversion of a capillary vessel into an AV shunt. Our data advocate for further investigation into the mechanisms regulating EC volume in health and disease as a way to identify therapeutic approaches to prevent and revert AVMs.
Keywords	Angiogenesis • Arteriovenous malformations • Cell volume • Oxygen-induced retinopathy

1. Introduction

Arteriovenous malformations (AVMs) form as a consequence of the maladaptive organization of blood vessels. They are defined as abnormal high-flow connections between an artery and a vein bypassing the capillary bed.[1,2] These characteristics lead to reduced tissue oxygenation and to high risks of haemorrhages and ruptures, which are often fatal when occurring in the brain. The majority of brain AVMs are a consequence of sporadic events (∼95%), yet familial cases exist (∼5%).[2] A significant number of all sporadic cases have been linked to somatic mutations in genes associated with the RAS-MAPK pathway.[3,4] Congenital forms are particularly associated with hereditary haemorrhagic telangiectasia (HHT), a rare autosomal dominant genetic disorder.[5,6] HHT is caused predominantly by *ACVRL1* and *ENG* mutations[7–9] but can also be associated with mutations on *SMAD4*[10,11] or *GDF2*.[12–15]

Recent advances in mouse and zebrafish animal models have provided novel insights into the mechanisms of AVM formation and progression. A common characteristic seems to be the cellular origin of these vascular

malformations, which have been mapped to venous or capillary beds.[16–18] Another common feature is the requirement of blood flow as a driving force for AVM development.[19–24] Yet, despite these recent advances, the cellular and molecular mechanisms leading to AVM formation remain unclear. Several reports have highlighted that increased sensitivity to VEGF signalling and concomitant endothelial cell (EC) proliferation are core features of BMP loss-of-function (LOF)-related AVM development, and interventions blocking EC proliferation such as VEGF, PI3K, AKT, or mTOR inhibitors can prevent the development of retinal AVMs in HHT mouse models.[21,25–27] In KRAS gain-of-function (GOF), ECs showed increased cell size, ectopic sprouting, and migration properties.[4,28] These behaviours are sensitive to MAPK inhibition but not to PI3K inhibition.[28] Alongside, changes in cell shape have also been suggested to contribute to AVM development both in mouse and zebrafish models.[29,30] More recently, defective flow-migration coupling, characterizing the ability of ECs to polarize and migrate against the blood flow direction, has been linked to HHT-like AVM models.[17,21,30,31] However, other reports showed no issues with flow-migration coupling.[16,32] Thus, to date, we lack a consensus model for AVM development and progression that could integrate all these observations and that would clarify why sporadic and familial cases develop similar vascular malformations despite arising from mutations impinging on very different signalling pathways.

2. Methods

2.1 Mice

All animal experiments carried out in this work were performed in compliance with the relevant laws and guidelines that apply to the Instituto de Medicina Molecular (iMM)—João Lobo Antunes, Faculty of Medicine, University of Lisbon, Portugal. Animal procedures were performed under the Direção-Geral da Alimentação e Veterinária (DGAV) project licences 012092/2016 and 017722/2021.

Mice were maintained at the iMM under standard husbandry conditions (under specific pathogen-free conditions and kept in individually ventilated cages) and under national regulations.

The following transgenic mouse strains were used in this study: GNrep,[33] *Arpc4* floxed,[34] *Srf* floxed,[35] *Alk1* floxed,[24] and R26-mTmG.[36] The different strains were crossed with Cdh5(PAC)-CreERT2[37] or Pdgfb-CreERT[38] to obtain the desired genotypes. Cre-negative littermates were used as controls in KO strain experiments. Both males and females were used, without distinction. At least two different litters were used for each experiment. Animals were sacrificed by decapitation before postnatal day (P) 18 and cervical dislocation or CO_2 inhalation for animals older than P18. Eyeballs were collected at different endpoints. Eyes were collected and fixed with 2% PFA (15710, Electron Microscopy Sciences) in PBS for 4 h at 4°C or in 4% PFA in PBS for 1 h at 4°C.

2.2 Treatments

4-Hydroxytamoxifen (H6278, Sigma-Aldrich) was injected intraperitoneally (IP) (20 µg/g) at different ages depending on the mouse strain and studied AV shunt stage. KO strains were injected at post-natal day 8 (P8) and P10 to study AV shunt formation or at Day 1 (P12) and Day 2 (P13) to study AV shunt resolution. GNrep mice were injected at P1 and P3 to trigger reporter expression. To trigger mosaic recombination in R26-mTmG, a low dose of 4-hydroxytamoxifen (0.4 µg/g) was injected IP only once at P8. Non-OIR pups were injected with the same low dose of 4-hydroxytamoxifen 3 days before the day of collection.

To block cell proliferation during shunt formation, mitomycin C (SC-3514B, ChemCruz) was injected IP (10 µg/g) at P4, and the mice were sacrificed at late P5 or Day 0, Day 1, and Day 2, and retinas were collected on Day 2 and 3. PBS was injected in control pups.

To access proliferation, *in vivo*, a stock of 50 mg 5-ethynyl-2-deoxyuridine (EdU) (Alfagene, A10044) was diluted in 5 mL of PBS to make a working solution (10 mg/mL). EdU solution was injected IP (200 µg/g) 4 h before the animals were sacrificed. Retinas were isolated and fixed as previously described, and the EdU-positive cells were detected according to the user manual of the Click-iT EdU Alexa Fluor 555 Imaging Kit (Invitrogen, C10338).

To affect glucose metabolism during shunt formation, PFKFB3 inhibitor (3PO; 50 µg/g) (525330, Merck Life Sciences) or 2-deoxy-D-glucose (2-DG; 500 µg/g) (25972, Merck Life Sciences) were injected IP at Day 0, Day 1, and Day 2, and pups were collected at Day 3. For both treatments, PBS was injected in control pups. mTOR pathway was inhibited using everolimus (13.5 µg/g) (73124, Stemcell) in peanut oil on Day 0, Day 1, and Day 2 to study shunt formation or at Day 3, Day 4 and Day 5 to study shunt regression. Ethanol (vehicle) diluted in peanut oil was injected to control pups.

Vascular perfusion was assessed by injecting 10 µL of DyLight 649-conjugated *Lycopersicum esculentum* (tomato) lectin (DL-1178-1, Vector Laboratories) intracardially (1 mg/mL) in anaesthetized pups (pentobarbital sodium, 0.8 mg/g, IP; Dechra, NDC 17033-085-25). The solution was allowed to circulate for a minimum of 5 min time before mouse sacrifice.

2.3 Hyperoxia chamber protocol

P8 pups and their nursing mothers were housed in a BioSpherix A-Chamber (BioSpherix) equipped with a ProOx 110 oxygen controller (BioSpherix). In the chamber, the animals were exposed to 75% oxygen level from P8 until their return to normal room air conditions at P11, also termed Day 0. Pups were sacrificed at the time point described above.

2.4 Immunofluorescence on mouse retinas

Retinas were dissected in PBS and stained according to previously established protocols.[39,40] Briefly, retinas were incubated on a rocking platform for 2 h at room temperature (RT) in Claudio's blocking buffer (CBB) consisting of 1% FBS (LTID 10500-064, Thermo Fisher Scientific), 3% BSA (MB04602, NZYtech), 0.5% Triton X-100 (T8787, Sigma-Aldrich), 0.01% sodium deoxycholate (30970, Sigma-Aldrich), and 0.02% sodium azide (S2002, Sigma-Aldrich) in PBS, pH = 7.4. Primary antibodies (see *Table 1*) were incubated in 1:1 CBB/PBS overnight on a rocking platform at 4°C. Afterwards, retinas were washed three times 30 min with PBS 0.1% Triton X-100 (×100, Sigma-Aldrich). Secondary antibodies (see *Table 1*) were incubated in 1:1 CBB/PBS overnight on a rocking platform in the dark at 4°C. Then retinas were washed three times 30 min with PBS 0.1% Triton X-100 and mounted on slides using Vectashield mounting medium (H-1000, VectorLabs).

Tile-scan spanning of retinas was acquired on either a Zeiss Cell Observer Spinning Disk confocal microscope equipped with ZEN Blue software or a 3i Marianas SDC spinning disk confocal microscope equipped with SlideBook 6.0.22 software. An EC plan-neofluar Ph1 ×10 NA 0.30 dry objective, a plan-apochromat Ph2 ×20 NA 0.80 dry objective, an LD C-apochromat Corr ×40 NA 1.10 water objective, and a plan-apochromat DIC ×40 NA 1.40 oil objective were used for the acquisitions. For EC volume, high-resolution images were obtained using a confocal laser point-scanning microscope (Zeiss 980) equipped with the ZEN software, using a plan-fluor apochromat ×63 NA 1.40 oil objective.

2.5 Image analysis

Most of the image analyses were performed with Fiji software.[41] AV shunt occurrence was quantified manually as a ratio between the total AV shunt observed over the total AV sections quantified at a specific time point in a specific condition. Only enlarged vessels connecting juxtaposed arteries, and veins were considered AV shunts. They are typically located along the angiogenic border between the vascularized and avascular zones at the centre of the retina.

Vessel density was calculated as a ratio between vessel area (CD31 mask segmentation) and total area. Endothelial cell density was defined as the number of ERG+ or GFP+ (GNrep mouse strain) nuclei (quantified manually) over the CD31 corresponding surface (determined after thresholding based on fluorescence intensity). Endothelial proliferation was quantified

Table 1 Antibodies

Antibody	Conjugation	Manufacturer	Reference	Dilution
Cleaved caspase-3	Unconjugated	Cell Signaling	1679664S	1/100
CD31	Unconjugated	R&D	AF3628	1/200
Donkey anti-Goat	Alexa Fluor 488	Thermo Fisher Scientific	A11055	1/400
Donkey anti-Goat	Alexa Fluor 555	Thermo Fisher Scientific	A21432	1/400
Donkey anti-Goat	Alexa Fluor 647	Thermo Fisher Scientific	A21447	1/400
Donkey anti-Rabbit	Alexa Fluor 488	Thermo Fisher Scientific	A21206	1/400
Donkey anti-Rabbit	Alexa Fluor 568	Thermo Fisher Scientific	A10042	1/400
Donkey anti-Rabbit	Alexa Fluor 647	Thermo Fisher Scientific	A31573	1/400
Donkey anti-Rat	Alexa Fluor 647	Thermo Fisher Scientific	A21434	1/400
Desmin	unconjugated	Abcam	ab15200	1/100
ERG	unconjugated	Abcam	ab92513	1/200
ERG	Alexa Fluor 647	Abcam	ab196149	1/75
GFP	FITC	Abcam	ab6662	1/400
Golph4	unconjugated	Abcam	ab28049	1/400
ICAM2	unconjugated	BD Biosciences	553326	1/100
KLF4	unconjugated	R&D	AF3158	1/20
mCherry	Alexa Fluor 594	Thermo Fisher Scientific	M11240	1/100
NG2	unconjugated	Merck Millipore	AB5320	1/100
pSmad1/5/9	unconjugated	Cell Signaling	13820	1/100
αSMA	Cy3	Sigma-Aldrich	C6198	1/400
SOX17	unconjugated	R&D	AF1924	1/50
VEGFR3	unconjugated	R&D	AF743	1/20
Dll4	unconjugated	R&D	AF1389	1/50

manually as a ratio of the number of EdU+/ERG or GFP double-positive cells over the corresponding number of ERG or GFP+ cells. Diameters were quantified using the VasoMetrics Fiji tool[42] with a 10 μm step between crosslines, and the average value was considered the diameter of the vessel. For arteries and veins, the diameter was measured within the range of 800–1200 μm from the optic nerve, as this region is expected to present shunts. In the case of shunts, arterioles, and venules, the entire vessel segment was measured.

Polarity was defined manually based on the angle of the nucleus-to-Golgi axis with estimated flow direction in three categories: with the flow (0–45°), random (45°–135°), and against the flow (135°–180°). Sprouts were quantified manually as the ratio of branch point number to a specific vessel (AV shunt or vein) over the length of that vessel. The neovascularized area was defined as the CD31 surface (after thresholding based on fluorescence intensity) over the proximal surface delimited by the AV shunt, its corresponding artery and vein, and the optic nerve.

Lectin perfusion was quantified in two different ways: (i) for neovascular area perfusion, it was defined as the lectin signal surface (after thresholding based on fluorescence intensity) over the proximal surface; (ii) for connection perfusion, it was quantified as a ratio between the number of branch points positive for lectin and the total number of branch points considered.

The avascular area of the AV shunts section in each retina was measured by using the 'polygon selection' tool and selecting capillary-free avascular area, near the optic nerve.

Cell volume was analysed using Imaris software (Oxford Instruments). High-resolution images of single mGFP+ EC were acquired using a 980 confocal microscope equipped with a ×63 NA 1.40 oil objective. The mGFP channel was segmented using the 'surfaces' segmentation tool to create a solid volume (see Supplementary material online, *Video S1* and Supplementary material online, *Figure S6*). The unsegmented signal arising from the low GFP signal at the nucleus was manually corrected using Fiji. ERG staining allowed discrimination between individual or clustered cells. Anatomic location was used to assign the identity of each cell (in the artery

or vein or in the capillary network next to an artery or vein). Quantification of cell volume in OIR conditions focused only on vessels next to the avascular zone, as changes in vessel diameter were more prominent in this region, and coincided with the location where AV shunts arise.

2.6 Blood flow simulations

Blood flow in the networks is treated as a continuous one-dimensional fluid, imposing Poiseuille's law at each segment, with additional empirical components for the Fåhraeus effect, Fåhraeus–Lindqvist effect, and non-proportional red blood cell partitioning at microvascular bifurcations. Full details of the method can be found in the literature.[43,44] The boundary conditions for the blood flow simulations were set as pressure conditions, with 68 mmHg at the inlet and 11 mmHg at the outlet.[39,45]

Normalizing the blood flow to the first venule is done through the following equation:

$$Q = \frac{Q1}{\sum_{i=1}^{n} Qi}$$

where Q is the normalized flow to the first venule, Q1 is the flow rate to the first venule, n is the number of venules in the network, and Qi is the flow rate of the venule. The Student's t-test is used to test if two distributions are statistically different or not. The null hypothesis of the test is that the mean of the two distributions is the same. If the null hypothesis is rejected, that is, the P-value from the test is below 0.05, and the two distributions have a different mean.

2.7 Scaling network

Between Day 0 and Day 1, there is a diameter growth in the microvascular networks. Given that the experimental protocol does not allow imaging of the same network over more than 1 day, we approach the characterization

Table 2 Relative growth in diameter of vessels between Day 0 and Day 1

Vessel	Relative growth
Vein	1.63
Venule 1	2.56
Venule 2	1.61
Venule 3	1.57
Venule 4	1.33
Artery	1.21
Arteriole 1	1.25
Others	1.50

of diameters by statistically comparing groups of Day 0 ($n = 11$) and Day 1 ($n = 10$) networks. *Table 2* summarizes the relative growth of the vessels in the networks between Day 0 and Day 1, where the growth of the 'all other vessels' is defined as the mean of the second, third, and fourth venule. To simulate how the Day 1 networks may have behaved haemodynamically at Day 0, and assuming a negligible change in the network topology, the Day 1 vessel diameters in the networks are scaled down by the relative growth in *Table 2*.

2.8 Statistical analysis

All statistical analyses were performed using RStudio (The R Foundation for Statistical Computing) and GraphPad Prism 8.4.2. Quantifications were done on independent samples. Each data point corresponds to the AV section, a vessel, a retina, or a single cell, and the number of animals per experiment and the number of litters are stated in the figure legend. Statistical details of experiments are reported in the figures and their legends. No inclusion, exclusion, or randomization criteria were used, and all analysed samples were included. Comparisons between the two experimental groups were analysed using Mann–Whitney test. Multiple comparisons between more than two experimental groups were assessed with Kruskal–Wallis test and combined with Dunn's *post hoc* test using Benjamini–Hochberg correction for *P*-value adjustment. Proportion comparisons were analysed using Fisher's exact *t*-test and combined with Fisher's *post hoc* test using Benjamini–Hochberg correction for *P*-value adjustment in the case of multiple comparisons. A result was considered significant when $P < 0.05$.

3. Results

3.1 Oxygen-induced retinopathy (OIR) model triggers transient non-genetic AV shunts

OIR is a protocol commonly used to model pathological angiogenesis, mimicking retinopathy of prematurity.[46,47] Briefly, neonatal mouse pups are exposed to hyperoxia promoting vascular regression and generating avascular retinal areas. Pups are then returned to normoxic conditions, leading to excessive and pathological neovascularization of the avascular regions. This response depends on the hypoxia-driven expression of the main pro-angiogenic factor VEGFA.[48] Our protocol involves placing mouse pups at post-natal day 8 (P8) in a hyperoxia chamber until P11 (*Figure 1A*), after which pups return to normoxic conditions. The day of return to normoxia is termed Day 0. Remarkably, we noted the rapid emergence of AV shunts in the retinal vascular network (*Figure 1A* and *B*). AV shunts always form between the juxtaposed arteries and veins in the mouse retina (see Supplementary material online, *Figure S1A*) and along the angiogenic border between the vascularized and avascular zone at the centre of the retina (see Supplementary material online, *Figure S1A* and *B*). For each visible

artery–vein pair, we determined the presence/absence of AV shunt and analysed the proportion of AV shunts per retina at specific time points. AV shunts appear starting 2 days (Day 2) after the return to normoxia (*Figure 1B*). AV shunt diameter is variable and has a maximum mean width at Day 3 (see Supplementary material online, *Figure S1C*). Interestingly, AV shunts start regressing at Day 5, and by Day 8 very few to none can be detected in retinas (*Figure 1B*). This is associated with a decrease in AV shunt diameter from its peak at Day 3 (see Supplementary material online, *Figure S1C*).

Next, we analysed OIR-induced AV shunts for characteristic features linked to genetically driven AVMs. Intracardiac injection of fluorescently labelled lectin in anaesthetized pups (pentobarbital sodium, 0.8 mg/g, IP) demonstrated that AV shunts are open and functional, sustaining direct blood flow between arteries and veins (*Figure 1C*). These AV shunts exhibit high αSMA+, NG2+, and desmin+ mural cell coverage (*Figure 1D* and Supplementary material online, *Figure S1D* and *E*), which may indicate a high-flow profile. This is further corroborated by high expression levels of KLF4 (*Figure 1E*), a shear stress-responsive transcription factor,[49] which was also described as highly expressed in HHT-associated AVMs.[32,50] Together, these results demonstrate that AV shunts are high-flow vessels that become muscularized, resembling genetically driven AVMs. Remarkably, despite these common characteristics, the AV shunts developed in this model are not a consequence of reduced ALK1 signalling. EC nuclei in the AV shunt show normal/higher levels of Smad1 phosphorylation in comparison to capillary vessels (*Figure 1E*), suggestive of ongoing BMP/ALK1 signalling. In addition, we investigated the EC identity of AV shunts (see Supplementary material online, *Figure S2*). Staining for SOX17 and DLL4 (arterial-enriched markers) and VEGFR3 (venous-enriched marker) in the OIR setting are not as segregated as in early retinal development.[51] Yet, arteries tended to show higher SOX17 and DLL4 levels and lower VEGFR3 levels when compared to veins (see Supplementary material online, *Figure S2*). Remarkably, the immunofluorescence signal in AV shunts more closely resembled arteries than veins, suggesting an arterialized AV shunt. Overall, we have identified and characterized a non-genetic model of AV shunt formation that phenocopies genetically driven AV shunts. We propose that this model allows investigation of both the formation and the regression of AVMs with high spatiotemporal resolution.

3.2 Non-genetic AV shunt formation is preceded by the enlargement of venules

Next, we analysed with higher temporal resolution the process of AV shunt formation. As AV shunts arise between Day 1 and Day 2, we collected retinas every 4 h from timed animals between 24 and 48 h. The first AV shunt started appearing at 32 h. Around 36 h, almost all retinas presented AV shunts, with around 40% of AV segments forming an obvious AV shunt (*Figure 2A* and *B*). This means that in around 8 h (from 28 to 36 h), a large proportion of capillaries connecting AV segments converted into an AV shunt (*Figure 2A* and *B*). Thus, we concluded that AV shunt formation is a progressive but rapid process. The speed of this process is similar to what is observed in Alk1-deficient mice, where AV shunts can be observed 24 h post-Alk1 inactivation.[7–9] To understand how such a quick conversion of capillaries into an AV shunt is possible, we studied the architecture of the vascular network during this time window (24–48 h). As shunts preferentially develop at the limit between the avascularized and the vascularized area (see Supplementary material online, *Figure S1A* and *B*), we characterized arteries and veins in this region. Artery and vein diameters increased prior to AV shunt formation when compared to diameters of vessels from animals at Day 0, immediately collected after the hyperoxia period (0 h) (see Supplementary material online, *Figure S3A* and *B*). At 24 h (Day 1), the artery mean diameter is ~121% (mean at Day 0 = 10.2 µm vs. Day 1 = 12.5 µm), and the vein diameter is ~163% (mean at Day 0 = 17.5 µm vs. Day 1 = 28.5 µm) bigger than Day 0 diameters (see Supplementary material online, *Figure S3A* and *B*). However, this change was not significant as there was a large variability between animals. This increase in vessel diameter continued over time, and by 32 h
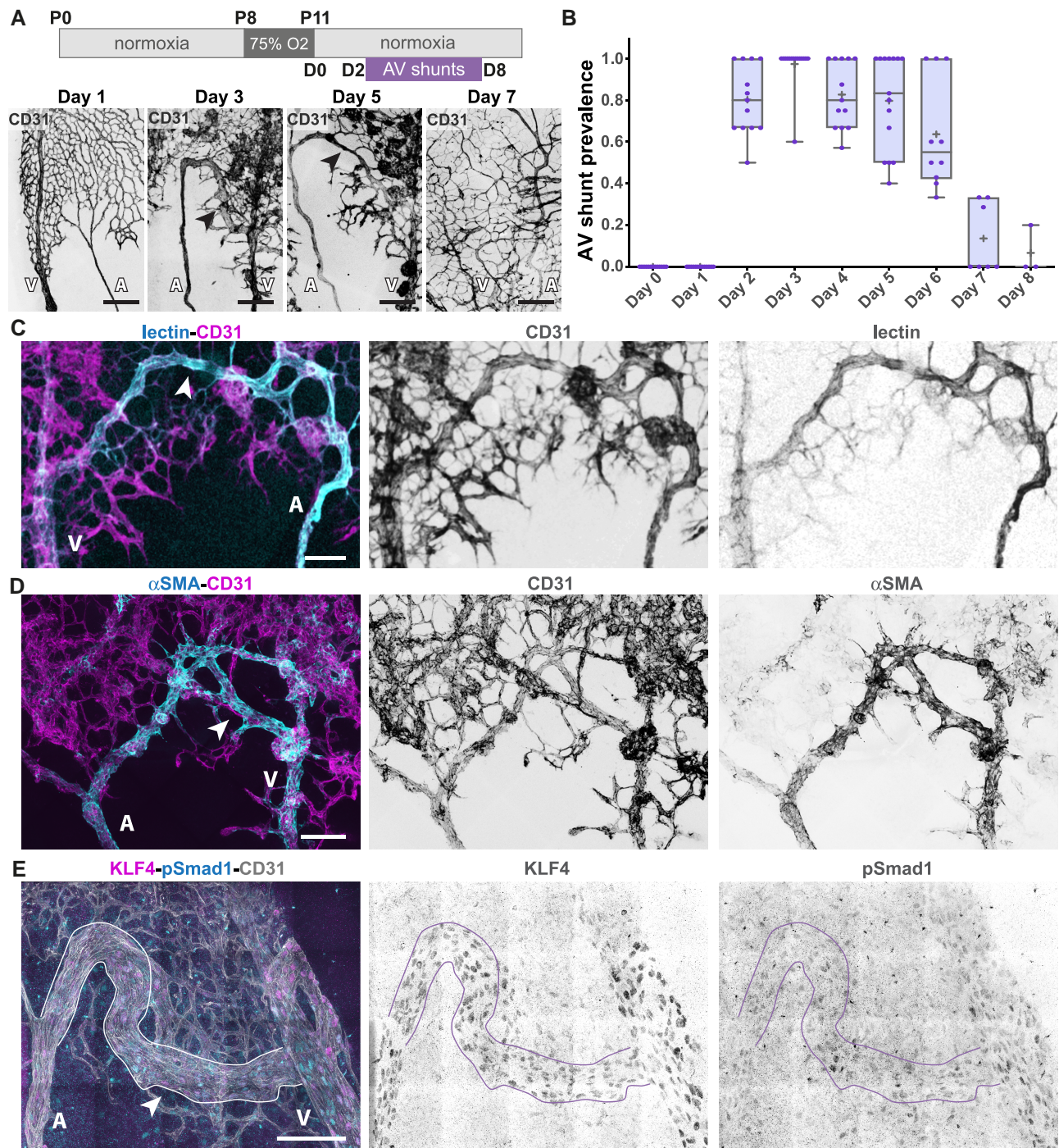
Figure 1 OIR protocol forms transient AV shunts independent of genetic alterations. (*A*) Top panel: schematic of the experimental protocol. Bottom panel: representative images of mouse retinas stained for CD31 (grey) on Day 1, Day 3, Day 5, and Day 7. Black arrows: AV shunt; A, artery; V, vein. Scale bar: 200 µm. (*B*) Quantification of AV shunt prevalence between Day 0 and Day 8. Day 0, 51 AV sections (8 pups); Day 1, 44 AV sections (8 pups); Day 2, 56 AV sections (8 pups); Day 3, 66 AV sections (8 pups); Day 4, 55 AV sections (7 pups); Day 5, 50 AV sections (7 pups); Day 6, 41 AV sections (6 pups); Day 7, 30 AV sections (4 pups); Day 8, 11 AV sections (3 pups). Each dot represents a mouse retina. (*C*) Representative image of an AV shunt at Day 3 highlighting its perfusion status (lectin, cyan) and co-stained for ECs (CD31, magenta). Arrowhead: AV shunt; A, artery; V, vein. Scale bar: 100 µm. (*D*) Representative image of smooth muscle coverage (αSMA, cyan) of an AV shunt at Day 4 co-stained for ECs (CD31, magenta). Arrowhead: AV shunt; A, artery; V, vein. Scale bar: 100 µm. (*E*) Representative image of an AV shunt at Day 3 stained for ECs (CD31, grey), pSmad1 (cyan), and KLF4 (magenta). Arrowhead: AV shunt; A, artery; V, vein. Scale bar: 100 µm.

changes became significant in veins and by 36 h in arteries (see Supplementary material online, *Figure S3B*). By 40 h, when most of the AV shunts have already developed, the artery mean diameter increased by ~166%, and the vein diameter by ~224% (see Supplementary material online, *Figure S3B*). Yet, remarkably, these effects were even more pronounced in vessel branches of veins. The diameters of vessels connecting to arteries (arterioles) and vessels connecting to veins (venules) increase more markedly before shunt formation, when compared to parent vessels (*Figure 2C* and *D* and Supplementary material online, *Figure S3B*). For instance, by 40 h, the arteriole mean diameter had increased by ~196% (mean at Day 0 = 7.0 µm vs. 40 h = 13.7 µm) and the venule diameter by ~290% (mean at Day 0 = 4.5 µm vs. 40 h = 13.0 µm) (*Figure 2D* and Supplementary material online, *Figure S3B*). Remarkably, the diameter of the first venule was already fully enlarged at 24 h, maintaining a stable vessel width over time, whilst the other venules and arterioles increased gradually and peaked at 32–40 h post-normoxia (*Figure 2C* and *D* and Supplementary material online, *Figure S3B*). Given that AV shunts tend to form at the first venous connection (see Supplementary material online, *Figure S1B*), these results suggest that structural adaption of the first venules precedes AV shunt formation.

Given that blood flow is required for AVM formation,[19,20,22,23,52] we hypothesize that OIR-dependent venule diameter increase predisposes capillary vessels to develop AV shunts by promoting unregulated blood flow between high-flow segments (proximal arteries and veins). To investigate this hypothesis, we used blood flow modelling to assess any imbalance in flow distribution in OIR retinal vascular networks. We started by comparing the normalized blood flow rate to the first venule in Day 0 and Day 1 networks. We observed that in Day 0 networks, the first venule receives a mean normalized flow rate of 1.2, indicating that the first venule captures a fraction of flow almost proportional to the number of venules in the network (see Supplementary material online, *Figure S3C* and *D*). On the other hand, we detected that the first venule in the Day 1 networks has a mean normalized flow rate of 2.34, indicating it significantly captures a disproportionately high flow rate (see Supplementary material online, *Figure S3C* and *D*). We hypothesize that this increase in flow to the first venule in Day 1 networks is a result of the relative diameter growth of the first venule being higher than that of the other venules (*Figure 2D* and Supplementary material online, *Figure S3B*). To test that hypothesis, we scale down the Day 1 networks by the inverse of their growth between Day 0 and Day 1 and perform the blood flow simulations in the scaled-down Day 1 networks. We observed that the first venule in the scaled-down Day 1 networks captures a similar normalized flow rate, 1.18, which is comparable (no statistical difference) to the Day 0 networks, 1.2 (see Supplementary material online, *Figure S3D*). These results indicate that the functional change between the Day 0 and Day 1 networks, that is, the first venule having a disproportionately high flow rate, is caused by the disproportional growth of the first venule. Furthermore, it indicates that a functional shunting of the network occurs before morphological shunting becomes strongly apparent.

3.3 Endothelial proliferation nor endothelial migration is involved in OIR-induced AV shunt formation

We next focused on the cellular mechanism leading to venule diameter increase on Day 1. First, we investigated EC proliferation, as it has been previously linked to AVM formation,[21,25–27] and that the OIR model is associated with neo-angiogenesis and extensive EC proliferation.[47] Indeed, we observed extensive EC proliferation in the different vessel beds on Day 3, assessed by the fraction of EdU+ ECs (*Figure 3A*). To assess the involvement of EC proliferation in AV shunt formation, we blocked cell proliferation using mitomycin C, a drug that inhibits DNA synthesis and cross-links DNA, effectively blocking the cell cycle.[53] We treated pups with mitomycin C at 0, 24, and 48 h post-normoxia and collected retinas at Day 3 (*Figure 3A*). Immunofluorescence for EdU demonstrates efficient abrogation of EC proliferation in mitomycin C-treated animals (*Figure 3A*,

Supplementary material online, *Figure S4A and B*). Accordingly, we observed a decrease in EC density in all vascular beds, including AV shunts, in mitomycin C-treated animals compared to PBS-treated mice (see Supplementary material online, *Figure S4C*). Yet, we observed no differences in the occurrence of AV shunts between PBS-treated and the mitomycin C-treated pups (*Figure 3B*), nor a difference in shunt diameter between the two groups (*Figure 3C*). Thus, we concluded that EC proliferation is not required for AV shunt formation in our model.

Next, we explored the role of EC migration in AV shunt development. Flow-migration coupling has been described as a player of AVM formation.[17,21] We analysed flow-migration coupling using the EC front-rear polarity GNRep mouse strain[33] (see Supplementary material online, *Figure S4D–G*). We found that at Day 0, there was a non-significant reduction in polarity patterns between staged non-OIR animals (P13) and Day 0, suggesting that the OIR protocol does not significantly affect polarity patterns in arteries and veins (see Supplementary material online, *Figure S4E*). Interestingly, rather than a decrease in polarity, we found a significant increase in the polarization patterns of ECs in arteries or veins, between Day 1 and Day 2, the period where AV shunts develop (see Supplementary material online, *Figure S4E*). In addition, ECs in AV shunts also showed a significant polarization against the flow direction (see Supplementary material online, *Figure S4F and G*). Overall, these results suggest that flow-migration coupling is not the main mechanism leading to the formation of OIR-induced AV shunts.

Next, we evaluated the contribution of EC migration in our model. We first used the endothelial-specific conditional KO of Arpc4 (*Arpc4*-iECKO) mouse line. Arpc4 is an essential subunit of the Arp2/3 complex, which creates branching actin networks that are fundamental for cell migration.[54] We previously demonstrated that Arpc4-deficient ECs showed impaired cell motility, efficiently blocking EC sprouting and EC migration in the mouse retina.[54] To avoid confounding effects, we induced *Arpc4* deletion, through tamoxifen injection, during the hyperoxia stage and collected retinas at Day 3 (*Figure 3D*). As expected, *Arpc4* endothelial-specific deletion decreases the number of neo-angiogenic vascular sprouts during the revascularization stage (see Supplementary material online, *Figure S4H*), consistent with the essential role of Arp2/3 complex in cell migration and invasion.[54] Remarkably, inhibition of cell motility led to a small, but significant, reduction in the ratio of AV shunt formation at Day 3 (*Figure 3E*). Yet, inhibition of the Arp2/3 complex did not affect the diameter of existent AV shunts (*Figure 3F*). To further confirm these results, we additionally targeted SRF in ECs. Alongside the Arp2/3 complex, SRF is essential for EC migration, tip cell invasion, and vessel development.[55–57] We used a similar protocol to inhibit SRF in ECs as for Arpc4, using the *Srf*-iECKO mouse line. Consistently, *Srf* endothelial-specific deletion decreased the number of neo-angiogenic vascular sprouts during the revascularization stage (see Supplementary material online, *Figure S4I*). Yet, contrary to Arp2/3 complex inhibition, we did not observe a significant reduction in the percentage of AV shunts being formed at Day 3 in *Srf*-iECKO animals (*Figure 3G* and Supplementary material online, *Figure S4J*). In addition, *Srf* endothelial deletion significantly decreased the diameter of AV shunts (see Supplementary material online, *Figure S4K*), suggesting additional effects besides inhibition of cell migration.

Altogether, these combined results indicate that EC migration may contribute, but it is not essential for AV shunt formation or development.

3.4 EC volume changes drive AV shunt formation

Given that neither cell migration nor cell proliferation played major roles in AV shunt formation, we hypothesize that imbalances in EC distribution may cause enlargements of vessels. To examine this aspect, we decided to analyse cell density between Day 0 and Day 1 in different vascular beds, a stage preceding AV shunt formation. Within this time window, all vessel beds increase their diameters, with the first venule connection showing the highest increase in vessel diameter (*Figure 2D* and Supplementary material online, *Figure S3B*). We quantified the number of ECs per vessel area in different vessel segments to determine local EC
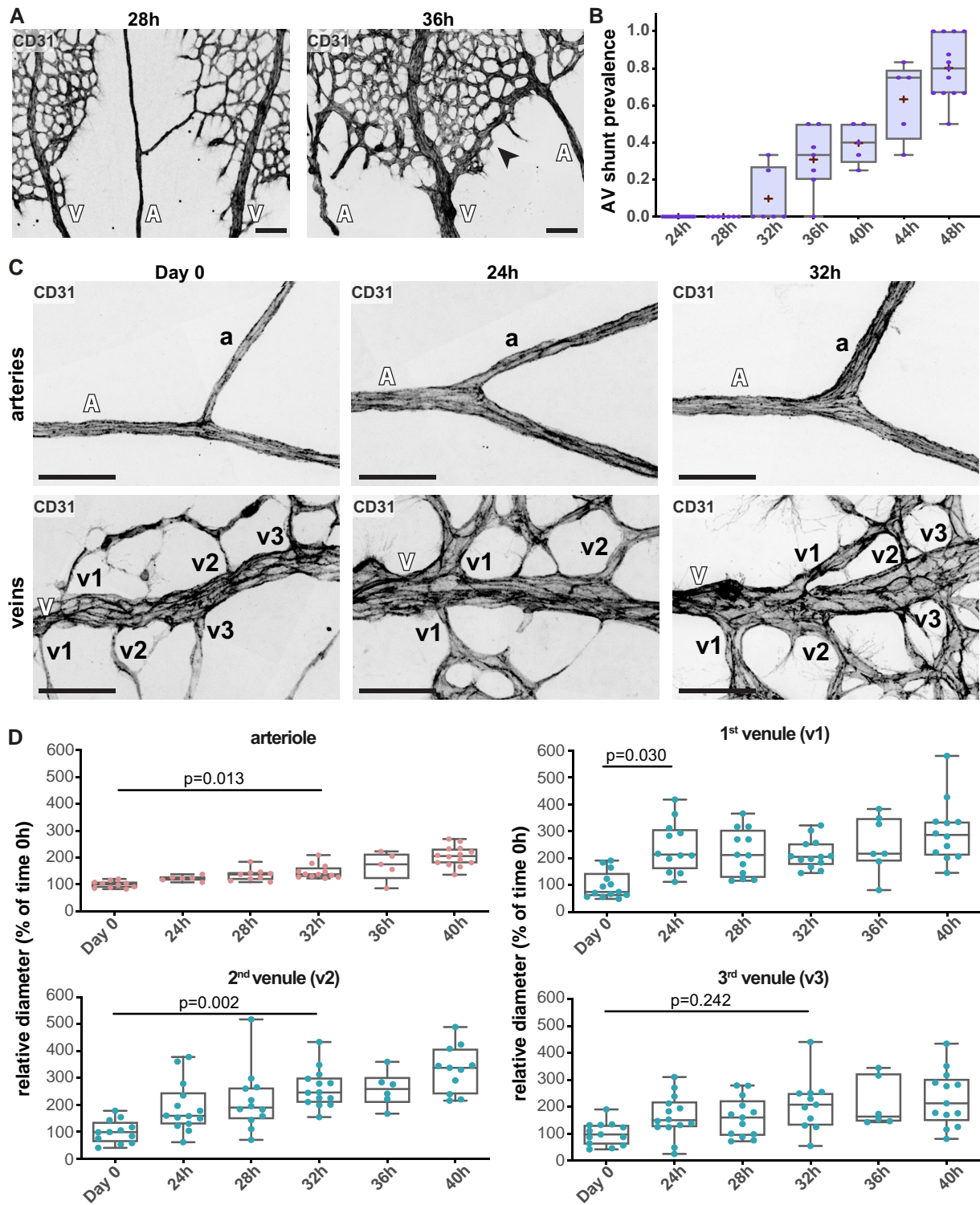
Figure 2 Fine time-course analysis of AV shunt formation. (*A*) Representative images of mouse retinas at 28 and 36 h stained for CD31 (grey). Black arrow: AV shunt; A, artery; V, vein. Scale bar: 200 μm. (*B*) Quantification of total AV shunt prevalence every 4 h between 24 and 48 h. 24 h, 44 AV sections (8 pups); 28 h, 31 AV sections (7 pups); 32 h, 29 AV sections (5 pups); 36 h, 34 AV sections (5 pups); 40 h, 23 AV sections (3 pups); 44 h, 23 AV sections (3 pups); 48 h, 56 AV sections (8 pups). Each dot represents a mouse retina. *P*-values from Fisher's exact *t*-test and Fisher's *post hoc* test using Benjamini–Hochberg correction for multiple comparisons. (*C*) Representative images of OIR arterial (top) and venous (bottom) mouse retina vessels (A, artery; a, arteriole; V, vein; v, venule) at 0, 24, and 32 h stained for CD31 (grey). Scale bar: 50 μm. (*D*) Quantification of arteriole and first (v1), second (v2,) and third (v3) venule normalized diameter (% of mean diameter at Day 0) between 0 and 40 h. Each dot represents a second-order vessel from Day 0 (3 pups); 24 h (3 pups); 28 h (3 pups); 32 h (3 pups); 36 h (3 pups); and 40 h (3 pups). Each dot represents a mouse retina. *P*-values from Kruskal–Wallis test and Dunn's *post hoc* test using Benjamini–Hochberg correction for multiple comparisons.
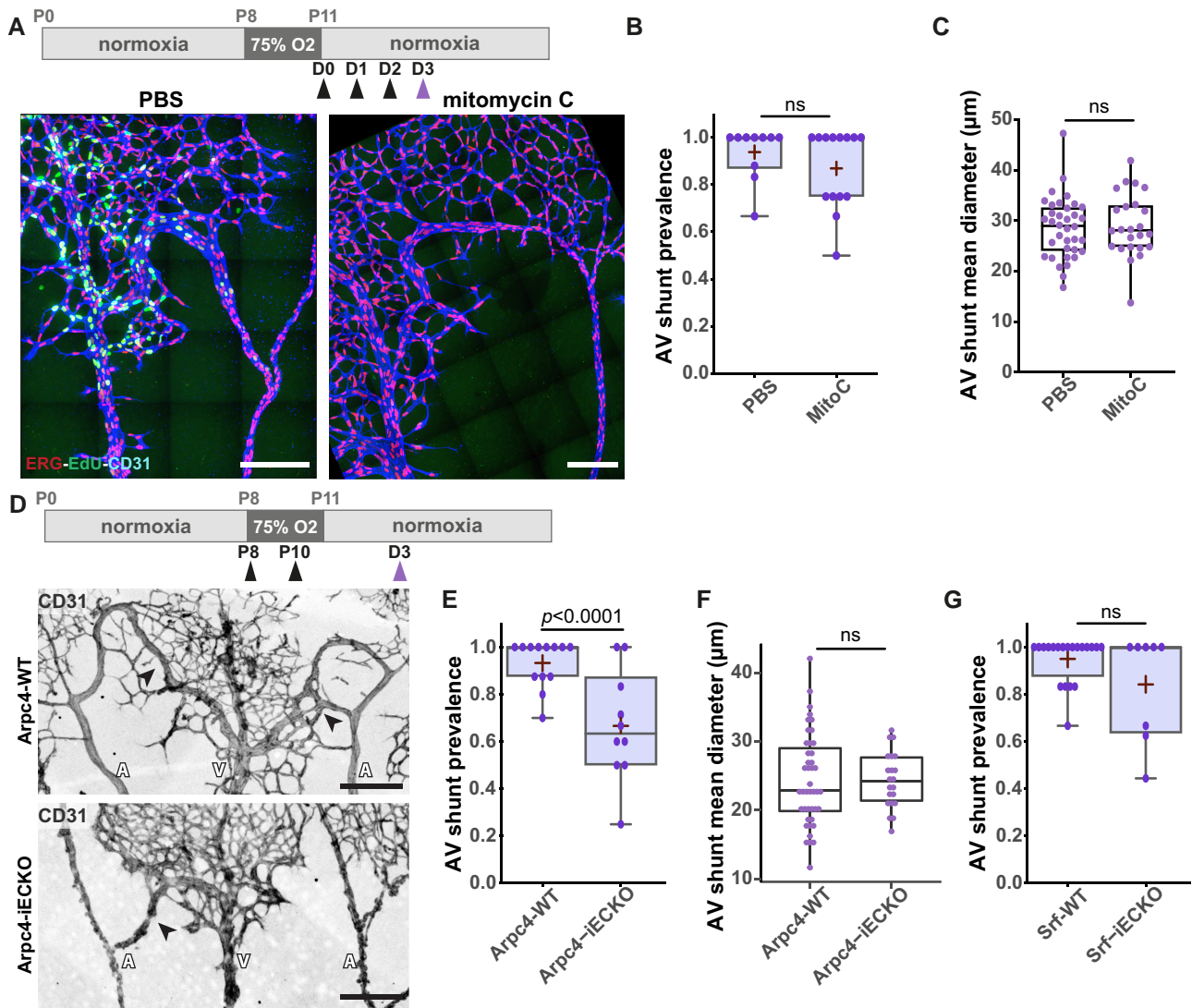
Figure 3 EC proliferation and migration have minor contributions to AV shunt formation. (*A*) Top panel: schematic of mitomycin C treatment. Black arrow: time of vehicle or mitomycin C injection. Purple arrow: time of collection. Bottom panel: representative images of retinas at Day 3 treated with PBS or mitomycin C stained for ECs (CD31, blue), EC nuclei (ERG, red), and proliferative cells (EdU, green). White arrows: AV shunts; A, artery; V, vein. Scale bar: 200 μm. (*B*) Quantification of AV shunt prevalence at Day 3 in PBS- (33 AV sections, 5 pups) and mitomycin C (46 AV sections, 7 pups)-treated retinas. Each dot represents a mouse retina. *P*-value from Mann–Whitney *U* test. (*C*) Quantification of AV shunt mean diameter at Day 3 in PBS- (21 AV sections, 3 pups) and mitomycin C (14 AV sections, 3 pups)-treated retinas. Each dot represents a mouse retina. *P*-value from Mann–Whitney *U* test. (*D*) Top panel: schematic of the experimental protocol using Arpc4/Srf mouse strains. Black arrow: tamoxifen injection. Purple arrow: time of collection. Representative images of Arpc4-WT and Arpc4-iECKO retinas on Day 3 stained for ECs (CD31, grey). Black arrows: AV shunts; A, artery; V, vein. Scale bar: 200 μm. (*E*) Quantification of AV shunt prevalence at Day 3 in Arpc4-WT (91 AV sections, 7 pups) and Arpc4-iECKO (57 AV sections, 5 pups) retinas. Each dot represents a mouse retina. *P*-value from Mann–Whitney *U* test. (*F*) Quantification of AV shunt mean diameter at Day 3 in Arpc4-WT (7 pups) and Arpc4-iECKO (5 pups) retinas. Each dot represents an AV shunt. Each dot represents a mouse retina. *P*-value from Mann–Whitney *U* test. (*G*) Quantification of AV shunt prevalence at Day 3 in Srf-WT (85 AV sections, 12 pups) and Srf-iECKO (45 AV sections, 5 pups) retinas. Each dot represents a mouse retina. *P*-value from Mann–Whitney *U* test.

density (*Figure 4A* and *B* and Supplementary material online, *Figure S5A*). Interestingly, the increase in vessel diameter in arteries, veins, and capillaries (either on the arterial or venous side) correlated with a significant decrease in EC density (*Figure 4B*). Remarkably, this effect was particularly strong in capillaries connecting to veins (*Figure 4B* and Supplementary material online, *Figure S5A*). These observations suggest that the increase in vessel diameter is likely a consequence of cell volume changes rather than an increase in the number or redistribution of ECs, through proliferation or migration. This hypothesis fits with the low impact of inhibition of proliferation or cell migration on AV shunt formation (*Figure 3A–C*). To assess whether cell volume increases before shunt formation, we stochastically activated Cre recombinase, using a low dose of tamoxifen, to promote the expression of membrane-bound GFP in retinal ECs, and analysed cell shape and cell volume at the single-cell level on Day 1 networks, before

AV shunt formation (*Figure 1B*). For this, we crossed the R26-mTmG mouse line with the Cdh5-CreERT[2] line,[36,37] and we used previously established protocols.[55,58,59] We segmented the membrane GFP signal to generate a solid object, and we analysed cell morphology and measured the total volume for each object (see *Supplementary material online, Figure S6A* and *Supplementary material online, Video S1*). Regarding cell shapes, no significant changes in the morphology of cells could be observed, with Day 1 cells displaying similar shapes to Day 0 cells (*Figure 4C*, *Supplementary material online, Figure S6A*). Notably, we observed a significant increase in cell volume for ECs in all vascular beds at Day 1 (*Figure 4C* and *D* and *Supplementary material online, Figure S6A–C*). Remarkably, the increase in cell volume is much more prominent on the venous side (~200% increase; Day 0 mean = 1123 μm^3 to Day 1 mean = 2332 μm^3 for veins and Day 0 mean = 1210 μm^3 to Day 1 mean = 2332 μm^3 for venous capillaries) than on the arterial side (~125% increase; Day 0 mean = 946 μm^3 to Day 1 mean = 1227 μm^3 for arteries and Day 0 mean = 1062 μm^3 to Day 1 mean = 1390 μm^3 for arterial capillaries) of the vascular tree (*Figure 4D* and *Supplementary material online, Figure S6C*). This effect was not due to abnormal EC volume at Day 0, as cell volumes are equivalent between cells from Day 0 and non-OIR retinas in any of the vascular beds (see *Supplementary material online, Figure S6D*). This effect correlates well with the bigger increase in vessel diameter on the venous side (*Figure 2D* and *Supplementary material online, Figure S2A*). Collectively, these results point in favour of the enlargement of venule connections and AV shunt formation stems from an increase in EC volume on the venous side.

To confirm this hypothesis, we used pharmacological inhibitors to block key metabolic pathways known to be involved in angiogenesis and cell volume control. First, we targeted glucose, as angiogenic ECs use glycolysis as the main source of energy.[60] To do so, we use 2-DG, which acts as a competitive substrate for hexokinase, inhibiting ATP production from glucose.[61] Remarkably, no significant changes in AV shunt formation or AV shunt diameter were observed (see *Supplementary material online, Figure S7A–C*). Next, we used an inhibitor of PFKFB3 (3PO), a key glycolytic enzyme, which was identified as being critical to vessel formation and a regulator of tip and stalk cell behaviour.[62] Similar to the 2-DG treatment, we observed no significant changes in AV shunt formation or AV shunt diameter were observed (see *Supplementary material online, Figure S7A–C*). Thus, we concluded that glycolysis does not regulate AV shunt formation. Next, we tested the inhibition of the mammalian target of rapamycin (mTOR), a key protein complex regulating cell metabolism, cell growth, and cell proliferation.[63] We used everolimus, which preferentially targets mTOR complex 1 (mTORC1).[63] Also, mTOR inhibitors were previously shown to prevent AVM in a mouse model of HHT.[27] A single dose of everolimus at Day 0 significantly decreased EC volume at Day 1, normalizing it to volumes similar to Day 0 cells. Daily injections of everolimus between Day 0 and Day 2 maintained normalization of EC volumes at Day 3 (*Figure 5A* and *B*). Importantly, everolimus-induced normalization of EC cell volumes correlated with a significant decrease in the rate of AV shunt development at Day 3 (*Figure 5C* and *D*), alongside a significant decrease in shunt diameter (*Figure 5E*), suggesting that a change in EC volume is an essential step initiating AV shunt formation in our mouse model. Moreover, everolimus treatment also normalized excessive αSMA+ and desmin+ mural cell coverage in the AV shunt area (see *Supplementary material online, Figure S7D*).

Taken together, our results collectively suggest a model describing the formation of an AV shunt (*Figure 5F*). We propose that AV shunts originate from the abnormal and asymmetric enlargement of venous vessels (*Figure 2*) due to an increase in EC volume (*Figure 4*) as the main cellular mechanism. This asymmetric vessel enlargement (*Figure 2*) promotes abnormal high flow rates (see *Supplementary material online, Figure S3C*) in the proximal capillary bed connecting arteries and veins, which correlates with the interface with the avascular zone in the OIR model. This initial uncontrolled flow pattern self-amplifies by the conversion of a capillary vessel path into a proper AV shunt. These later events will likely involve EC migration and EC proliferation, in addition to EC volume changes.

3.5 Genetically induced AV shunts arise independently of EC proliferation and depend on venous EC volume changes

To test if the proposed model applies to genetic models of AVMs, we focused on *Alk1* LOF in ECs. Endothelial-specific deletion of *Alk1* leads to rapid (30–60 h) development of AV shunts in the mouse retina.[24,64] Concordant with our data on OIR-induced AV shunts, we observed a significant increase in vessel diameter before AV shunt formation (*Figure 6A*). This increase was more robust on the venous side, when compared to the arterial side (*Figure 6A*), further corroborating the data obtained on the OIR model (*Figure 4D*). Next, to confirm if vessel diameter increase was associated with changes in cell volume, we intercrossed the Alk1 mouse model with the R26-mTmG mouse line. Low-dose tamoxifen injection allows recombination of a few ECs, enabling the measurement of the effect of Alk1 LOF in cell volume without generating AV shunts (see *Supplementary material online, Figure S7E*). We used Alk1 heterozygous cells as a control. Strikingly, stochastic recombination of Alk1 leads to a significant increase in EC volume at 72 h post-recombination specifically in the venous regions (*Alk1* KO mean 1323 μm^3 vs. *Alk1* het mean 721 μm^3), whilst the arterial ECs showed no significant changes (*Alk1* KO mean 906 μm^3 vs. *Alk1* het mean 810 μm^3) (*Figure 6B* and *C*). To further confirm that EC proliferation does not affect AV shunt formation in the *Alk1* LOF model, we co-injected mitomycin C together with tamoxifen to concomitantly induce Alk1 LOF and cell cycle inhibition (*Figure 6D*). Remarkably, we observed that the mitomycin C Alk1 LOF mouse retinas showed a high prevalence of AV shunts, to a level comparable to PBS-treated Alk1 LOF mouse retinas (*Figure 6E*). This further supports the idea that EC volume change is a primary driver of AV shunt formation rather than EC proliferation. Thus, we concluded that Alk1 signalling controls EC volume in a cell-autonomous manner and that the initiation steps driving AV shunt formation share similarities between HHT-induced and OIR-induced models.

In the OIR model, we showed that BMP/ALK1 signalling is active, as we observed substantial pSMAD1 staining (*Figure 1E*). Since OIR and Alk1 LOF could promote EC hypertrophy, we questioned if both experimental conditions activate a similar growth pathway or work via independent pathways. To test this, we subjected the endothelial-specific deletion of the *Alk1* mouse model to the OIR protocol. Given the short lifespan of Alk1-deleted animals, we analysed AV shunt prevalence at Day 2, as no LOF animal survived to Day 3. There was a slight tendency to increase in prevalence, but this tendency was not significant (see *Supplementary material online, Figure S7F and G*). We should remark that WT mice have already a high rate of conversion on Day 2. Nevertheless, EC volume analyses demonstrated that *Alk1* LOF venous ECs in the OIR model showed a significant increase in mean cell volume (1727 μm^3) compared to *Alk1* het venous ECs (1499 μm^3) in the OIR model, whilst arterial ECs showed no significant changes (*Alk1* KO mean 1215 μm^3 vs. *Alk1* het mean 1326 μm^3) (*Figure 6F*). This result suggests that BMP signalling inhibition synergizes with OIR-induced venous EC hypertrophy.

Overall, our data suggest that EC volume control, and concomitant flow pattern deregulation, is a key mechanistic step leading to AVM development also in HHT.

3.6 AV shunt regression is dependent on endothelial flow-migration coupling and cell volume changes but not on EC apoptosis

AV shunt regression is of clinical relevance yet very little is known about the underlying cellular and molecular mechanisms. Thus, we took advantage of the fact that OIR-induced AV shunts are not stable to investigate how AV shunts resolve. AV shunts start regressing at Day 5, and by Day 8 almost no AV shunts can be detected (*Figure 1B*). We hypothesize that shunt resolution could be the outcome of one or a combination of several mechanisms, including EC apoptosis, cell migration, or cell volume changes.
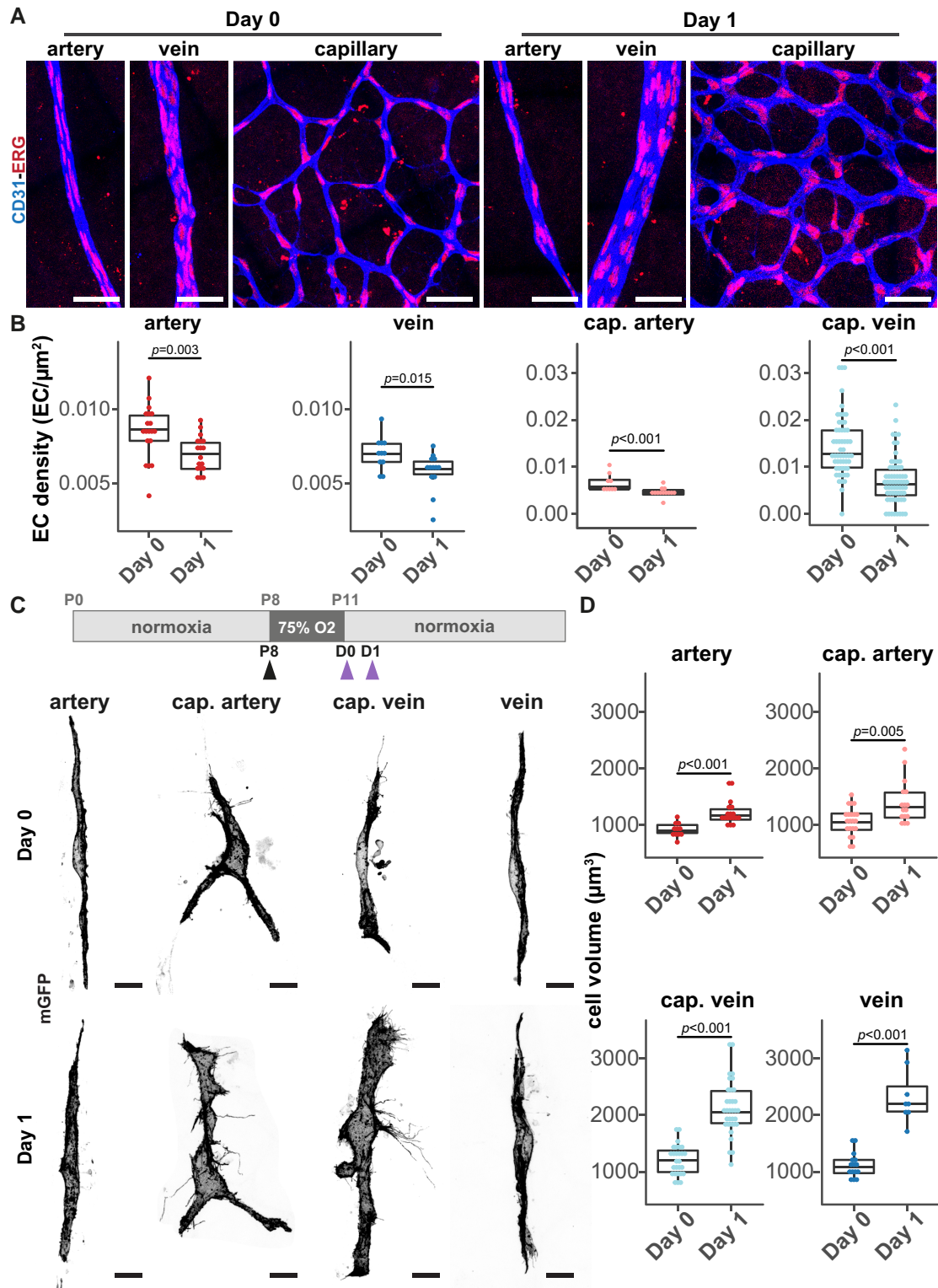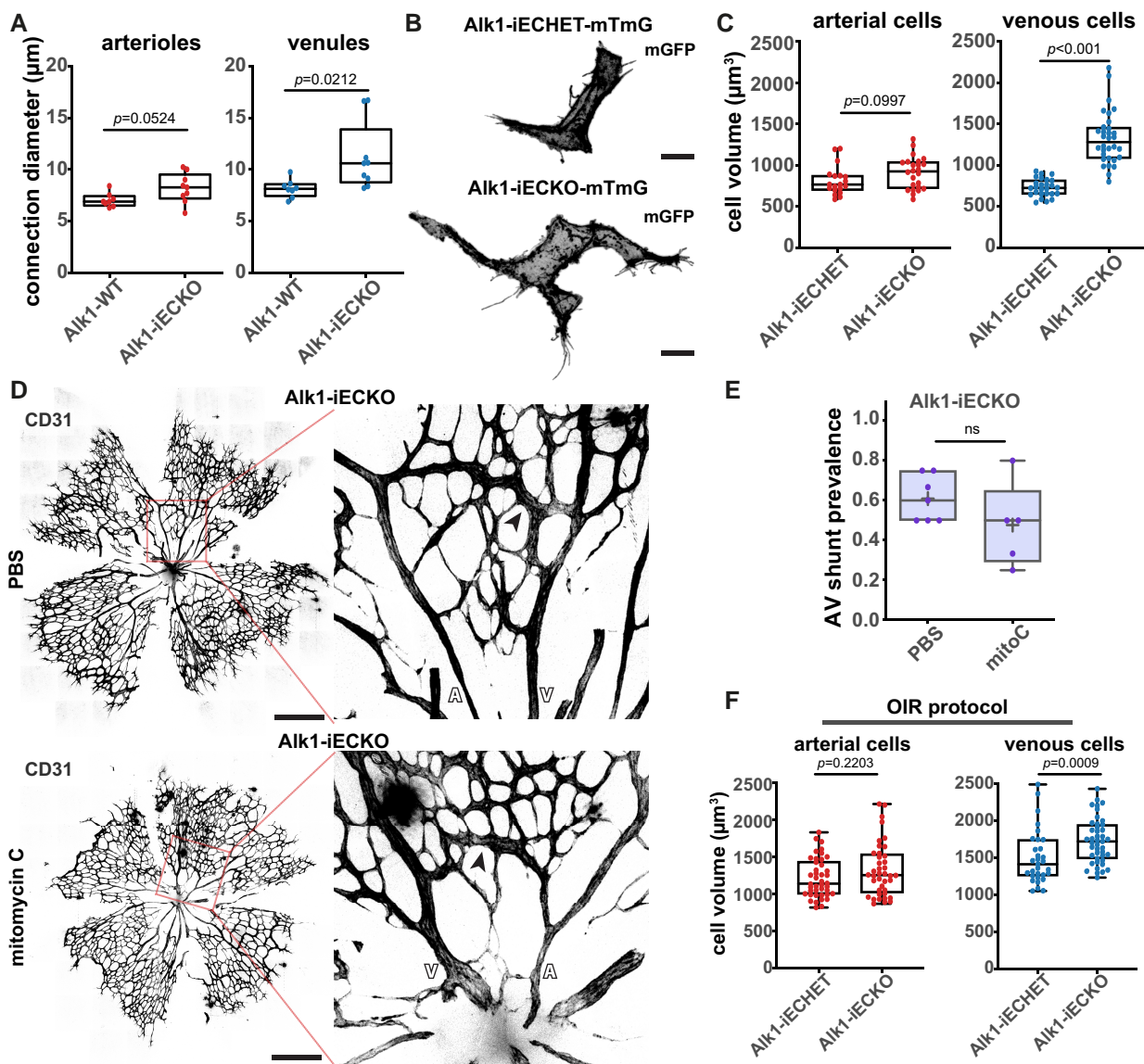
Figure 4 EC volume and venule diameter increases precede AV shunt development. (*A*) Representative images of EC nuclei (ERG, red) distribution within artery, vein, and capillary at Day 0 and Day 1 (CD31, blue). Scale bar: 50 μm. (*B*) Quantification of EC density in arteries, veins, arterial capillaries, and venous capillaries at Day 0 and Day 1. Each dot represents a vessel on Day 0 (4 pups) and Day 1 (5 pups). *P*-value from Mann–Whitney *U* test. (*C*) Top panel: schematic of experimental protocol for mosaic expression of mGFP in ECs. Black arrow: tamoxifen injection. Purple arrows: time of collection. Bottom panel: representative images of single ECs (mGFP, grey) in the artery, arterial capillary, venous capillary, and vein from mouse retinas at Day 0 and Day 1. Scale bar: 10 μm. (*D*) Quantification of EC volume in single cells in arteries, arterial capillaries, venous capillaries, and veins from mouse retinas at Day 0 and Day 1. Each dot represents an EC from Day 0 (11 artery, 21 cap. artery, 15 vein, and 25 cap. vein cells, 3 pups) and Day 1 (18 artery, 16 cap. artery, 8 vein, and 33 cap. vein cells, 3 pups). *P*-value from Mann–Whitney *U* test.
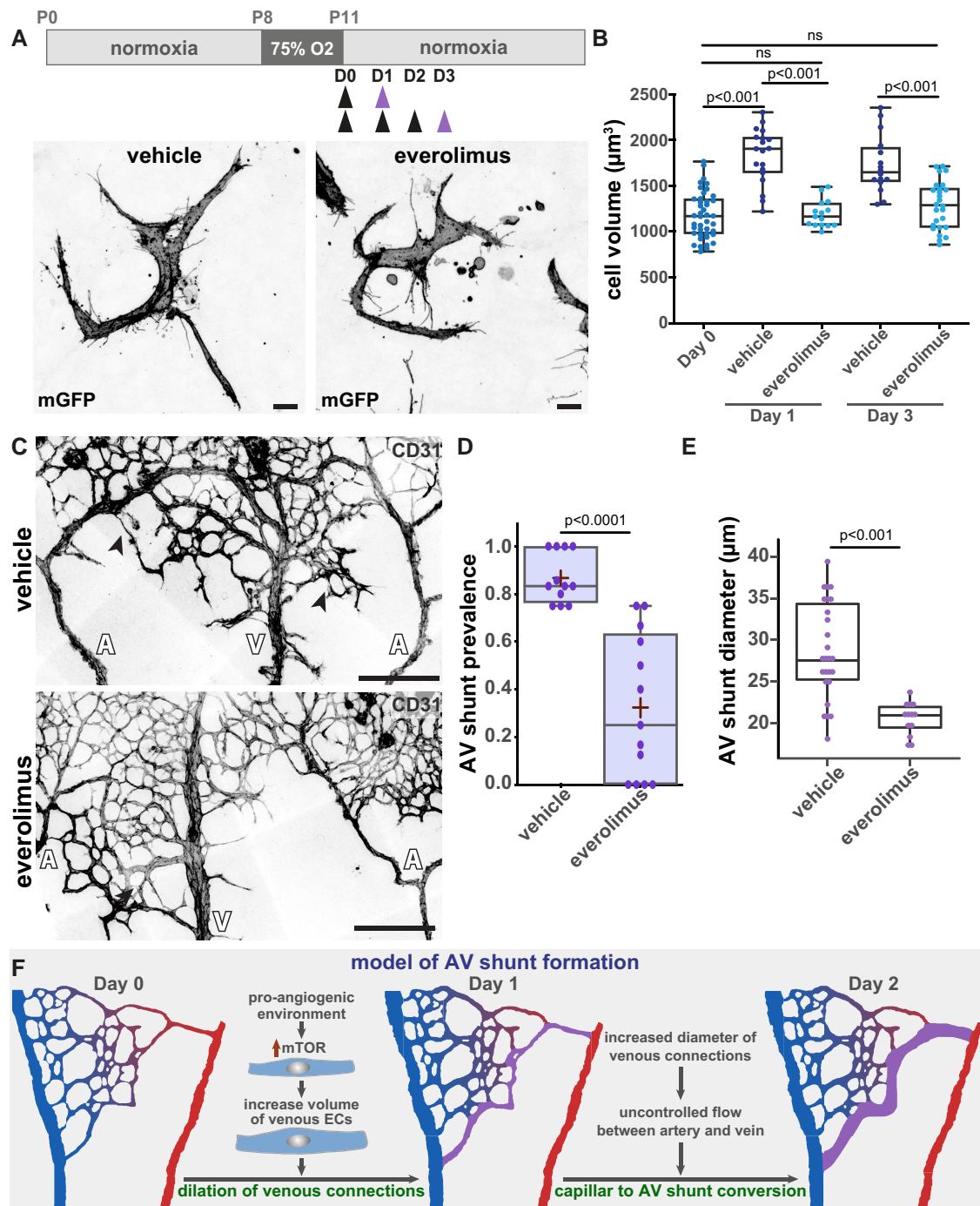
Figure 5 mTOR inhibition prevents EC volume increase and AV shunt formation. (*A*) Top panel: schematic of AV shunt study protocol with everolimus treatment. Black arrows: times of vehicle or everolimus injections. Purple arrow: time of collection. Bottom panel: representative images of single venous ECs (mGFP, grey) of retinas at Day 3 treated with vehicle or everolimus. Scale bar: 10 μm. (*B*) Quantification of EC volume in venous cells (veins and venous capillaries) at Day 0, Day 1, and Day 3 mouse retinas treated with vehicle or everolimus. Each dot represents one EC from Day 0 (42 cells, 3 pups), Day 1 (19 cells for vehicle and 15 cells for everolimus, 3 pups), and Day 3 (16 cells for vehicle and 26 cells for everolimus, 3 pups). *P*-value from Kruskal–Wallis test with Dunn's correction for multiple comparisons. (*C*) Representative images of retinas at Day 3 treated with vehicle or everolimus stained for ECs (CD31, grey). Black arrows: AV shunts; A, artery; V, vein. Scale bar: 200 μm. (*D*) Quantification of AV shunt prevalence at Day 3 in vehicle- (43 AV sections, 4 pups) and everolimus (54 AV sections, 5 pups)-treated retinas. *P*-value from Mann–Whitney *U* test. (*E*) Quantification of AV shunt mean diameter at Day 3 in vehicle- (4 pups) and everolimus (5 pups)-treated retinas. Each dot represents an AV shunt. *P*-value from Mann–Whitney *U* test. (*F*) Model describing AV shunt formation in OIR protocol.

Figure 6 Alk1 signalling controls EC volume cell-autonomously. (*A*) Quantification of arteriole and venule diameter in Alk1-WT (19 arterial and 24 venous cells, 4 pups) and Alk1-iECKO (24 arterial and 32 venous cells,4 pups) retinas 72 h post-tamoxifen injection. Each dot represents a second-order vessel. *P*-value from Mann–Whitney *U* test. (*B*) Representative images of ECs from a venous capillary EC (GFP, grey) of Alk1.iECHET-mTmG and Alk1-iECKO-mTmG 24 h post-tamoxifen injection. Scale bar: 10 µm. (*C*) Quantification of EC volume in arterial (arteries and arterial capillaries) and venous (vein and venous capillaries) vessels from Alk1.iECHET-mTmG and Alk1-iECKO-mTmG 72 h post-tamoxifen injection. Each dot represents one EC from Alk1.iECHET-mTmG (3 pups) and Alk1-iECKO-mTmG (3 pups). *P*-value from Mann–Whitney test. (*D*) Representative images (left, overview; right, higher magnification of the AV shunt) from Alk1-iECKO late P5 retinas treated with PBS or mitomycin C stained for ECs (CD31, grey). Black arrows: AV shunts; A:, artery; V, vein. Scale bar: 500 µm. (*E*) Quantification of AV shunt prevalence at Day 3 in Alk1-iECKO late P5 retinas treated with PBS (52 AV sections, 7 pups) or mitomycin (34 AV section, 5 pups). Each dot represents a mouse retina. *P*-value from Mann–Whitney *U* test. (*F*) Quantification of EC volume in arterial (arteries and arterial capillaries) and venous (vein and venous capillaries) vessels from Alk1.iECHET-mTmG and Alk1-iECKO-mTmG at Day 2. Each dot represents one EC from Alk1.iECHET-mTmG (42 arterial and 31 venous cells, 4 pups) and Alk1-iECKO-mTmG (40 arterial and 43 venous cells, 4 pups).

First, we investigated apoptosis, which could lead to a reduction in the number of ECs in a vessel segment leading to a decrease in its diameter. Active caspase-3 staining during the resolution phase highlights the existence of very few apoptotic ECs during this stage (see Supplementary material online, *Figure S8A*), and thus we excluded apoptosis as a mechanism for AV shunt resolution.

Next, we evaluated if cell dispersion through cell migration could explain AV shunt resolution. During this stage, we observed that shunt regression coincides with the neovascularization of the avascular area (*Figure 7A and B*).

This leads to an increase in the number of connections between the AV shunt and the parent arteries and veins and an increase in the vascular density of the neo-capillary network (*Figure 7A and B* and Supplementary material online, *Figure S8B*). Given that flow-migration coupling is essential for vascular remodelling and network optimization,[65–68] we hypothesize that redistribution of blood flow through the new vascular segments could reroute EC migration paths. This may decrease the number of ECs moving into AV shunts and therefore contribute to their normalization. As the majority of neo-vessels connect AV shunts with the adjacent veins (*Figure 7A and B*),

we predicted that this region may show the first signs of AV shunt normalization. To validate this hypothesis, we first assessed vascular perfusion of neovascular networks using intracardiac lectin injections in anaesthetized pups (pentobarbital sodium, 0.8 mg/g, IP). We observed a significant increase in the number of perfused vessel branches from both the vein and the AV shunt, from Day 2 to Day 6 (*Figure 7C* and *D*), suggesting progressive blood flow redistribution from AV shunts towards newly formed vascular beds. This coincided with an increase in the overall perfusion of the neovascular area (see Supplementary material online, *Figure S8C*). AV shunts start thinning and become less discernible at the venous side (*Figure 7A* and *C*), where the connection between the AV shunt and the draining vein becomes more entangled. Remarkably, quantification of AV shunt diameters from the arterial and venous sides showed a significant decrease in diameter in both arterial and venous sides starting at Day 5 (*Figure 7E*). Overall, these results strongly suggest that AV shunts regress due to changes in flow distribution and EC rerouting.

To tackle the importance of the blood flow redistribution and EC migration-flow coupling in AV shunt regression, we took advantage of the *Arpc4*-iECKO and *Srf*-iECKO mouse models to inhibit EC migration and invasion. To avoid any impact on the formation of AV shunts, we induced *Arpc4* or *Srf* deletion after return to normoxia. As expected, *Arpc4*-iECKO pups showed a significant reduction in the neo-angiogenic sprouts and a significant reduction in the vascularization of the avascular region (see Supplementary material online, *Figure S8D*). Remarkably, at Day 7, *Arpc4*-iECKO pups preserved AV shunts, contrary to control pups, where AV shunts almost completely regressed (*Figure 8A* and *B*). A similar trend was found when inhibiting SRF function in ECs. *Srf*-iECKO pups also showed a significant reduction in the number of neo-angiogenic sprouts (see Supplementary material online, *Figure S8E*), alongside the maintenance of AV shunts at Day 9 (*Figure 8C* and *D*). Altogether, we concluded that the formation of a neovascular network is essential for AV shunt regression.

Finally, we analysed EC volume. Given that an increase in EC volume is the driving force for AV shunt formation (*Figures 4* and *5*), we examined if the regression of AV shunts could correlate with a decrease in EC volume. To do so, we employed a similar approach as for AV shunt formation, with stochastic recombination of the reporter line at P8. The analysis of ECs in each vascular bed demonstrated normalization of cell volume in arterial and venous cells, obtaining volumes comparable to Day 0 (*Figure 8E*). To test if a decrease in EC volume could accelerate regression of established AV shunts, we injected everolimus for three consecutive days starting at Day 3 (see Supplementary material online, *Figure S8F*) and collected retinas for analysis at Day 6, a time point at which WT retinas showed still a high prevalence of AV shunts (*Figure 1B*). We found that there was no change in the AV shunt prevalence between vehicle- and everolimus-treated animals (see Supplementary material online, *Figure S8G*), suggesting that everolimus does not accelerate the spontaneous regression of OIR-induced AV shunts.

Thus, taken together, our data points towards a model where AV shunts resolve by a combination of EC dispersion through flow-migration coupling and EC volume normalization (*Figure 8F*). Both mechanisms may cooperatively promote the reversion of abnormally formed AV shunts into capillary vessels of normal diameter.

4. Discussion

In this work, we unravelled a new non-genetic mouse model to study AV shunt formation and regression with high spatiotemporal resolution. Through genetic and pharmacological interventions, we mechanistically demonstrated that EC volume control, rather than EC proliferation, is a key step in the formation of AV shunts, whilst a combination of cell volume control and EC flow-migration coupling is associated with the regression of these vascular malformations.

Based on our results, we propose a coherent and unifying timeline leading to the fast (24 h) conversion of a capillary vessel into an AV shunt. A first trigger, either genetic mutation or specific environmental conditions,

leads to hypertrophy of ECs and a concomitant increase in vessel calibre. Remarkably, our detailed analysis showed that the early changes driving both AV shunt development and regression are preferentially located in the venous compartment (veins and venous capillaries). This is in agreement with previous studies on HHT-associated AVMs that pointed towards ECs in capillaries or veins as the main cellular origin of vascular shunts.[16–18,21] This increase in cell volume is fuelled, at least partially, via the mTOR pathway, and it leads to the expansion of the capillary diameter. Our modelling work pointed out that, in turn, the expansion in vessel diameter decreases flow resistance leading to an increase in flow rates in the vessels prone to be converted into shunts. Increased levels of blood flow through these dilated vessels further expand the vessel lumen through a combination of EC migration, flow-migration coupling, and EC proliferation. Recruitment of αSMA-positive cells may promote the consolidation of the high-flow shunt. In addition, we showed that AV shunts can gradually regress through a combination of flow-migration coupling-induced remodelling and cell volume changes. The regression relies on the intrinsic capacity of ECs to migrate and rearrange within the vascular network to resolve maladaptive vessel configurations, an essential behaviour that we refer to as vascular plasticity.[68] In this context, the establishment of new vessel connections, which create new flow routes, is a prerequisite for AV shunt regression, and blockage of vascular plasticity can sustain environmentally driven AV shunts.

This detailed description of the initial steps in the formation and resolution of AVMs raises further questions. What is the relative contribution of EC volume control in shunt regression in relation to EC migration and EC redistribution? A large contribution of EC volume normalization would point towards a common cellular process involved in the genesis and resolution of these vascular anomalies, whilst a low contribution would indicate fundamentally different mechanisms of the two biological phenomena. The latter could indicate that known mutations driving AV shunts may impair two distinct cellular processes, one leading to EC volume increases and another disrupting vascular plasticity, which will promote the formation and, at the same time, prevent the mechanisms of regression.

One additional key question resides in the molecular mechanisms of EC volume control. So far, this question has raised very limited attention in the field of vascular biology. Yet, previous connections between cell size have been reported to be associated with AVM formation. For instance, HHT-driven mutations have been shown to lead to bigger EC sizes in zebrafish and mice.[29,30] Moreover, KRAS-activating mutations have recently been identified as the main driver of sporadic brain AVMs, and they were also associated with increases in EC volume.[4,28] However, constitutively active Notch4 also gives rise to AVMs with increased capillary diameters, yet cell volume changes have not been reported so far.[22,52,69] How these pathways regulate cell volume remains to be elucidated. Generally, short timescale cell volume control is achieved through osmolarity control, mainly via ion channels.[70,71] Longer timescale cell volume control has been mostly studied in the context of cell cycle and has been associated with several pathways promoting anabolism, such as the mTOR pathway,[63,72] MYC signalling,[73,74] the YAP/TAZ pathway,[75–77] and more recently cell mechanics.[78,79] Even if we cannot exclude the impact of osmolarity effects and short timescale fluctuations on cell volume, the significant normalization of EC volumes upon mTOR pathway inhibition with everolimus treatment (*Figure 5*), and concomitant impact on AV shunt formation, strongly suggests that anabolic activity is a key fundamental step in pathological EC volume control. How AVM-associated pathways regulate anabolism may differ according to the associated mutations. For instance, KRAS-activating mutations rely on MEK activity rather than on AKT/PI3K signalling, an upstream regulator of mTOR activity,[4,28] whilst ALK1, ENG, or SMAD4 LOF mutations showed sensitivity to AKT/PI3K signalling inhibitors.[21,25,26] In this regard, OIR-induced AV shunts are more closely related to HHT-associated lesions rather than to KRAS-induced AVMs. Remarkably, BMP pathway LOF mutations require pro-angiogenic environments to induce AVM formation whilst KRAS-activating mutations can promote AVM development in quiescent endothelium,[24,26,28,80] which further points towards a closer mechanistic relationship between OIR-induced AV shunts with HHT-associated AVMs. Outstandingly, the combination of
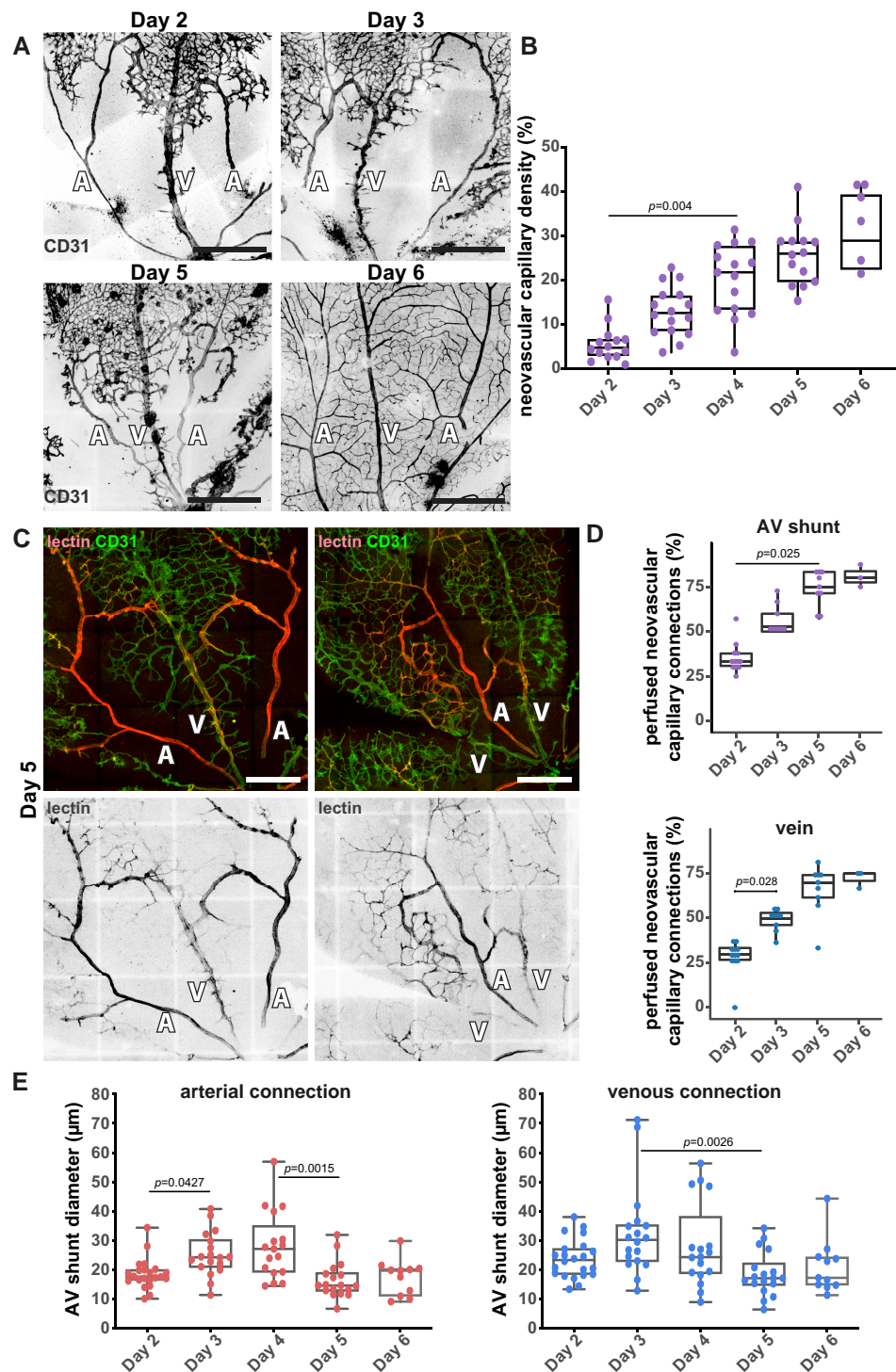
Figure 7 AV shunt regression associates with perfusion of the neo-capillaries. (*A*) Representative images of mouse retinas stained for CD31 (grey) at Day 2, Day 3, Day 5, and Day 6. A, artery; V: vein. Scale bar: 500 μm. (*B*) Quantification of neovascular capillary density between Day 2 and Day 6. Each dot represents an AV shunt proximal region from Day 2 (4 pups); Day 3 (3 pups); Day 4 (3 pups); Day 5 (4 pups); and Day 6 (3 pups). *P*-values from Kruskal–Wallis test and Dunn's *post hoc* test using Benjamini–Hochberg correction for multiple comparisons. (*C*) Representative images of Day 5 mouse retinas perfused with lectin (red) and co-stained for ECs (CD31, green). A, artery; V, vein. Scale bar: 250 μm. (*D*) Quantification of perfused neovascular capillary connections to AV shunt (top) and associated vein (bottom) between Day 2 and Day 6. Each dot represents an AV shunt or a vein from Day 2 (6 retinas); Day 3 (4 retinas); Day 5 (5 retinas); and Day 6 (3 retinas). *P*-values from Kruskal–Wallis test with Dunn's correction for multiple comparisons. (*E*) Quantification of AV shunt diameter on the first 50 μm connected to the corresponding artery (left) or vein (right) between Day 2 and Day 6 mouse retinas. Each dot represents an AV shunt from Day 2 (4 pups); Day 3 (3 pups); Day 4 (3 pups); Day 5 (4 pups); and Day 6 (3 pups). *P*-values from Kruskal–Wallis test and Dunn's *post hoc* test using Benjamini–Hochberg correction for multiple comparisons.
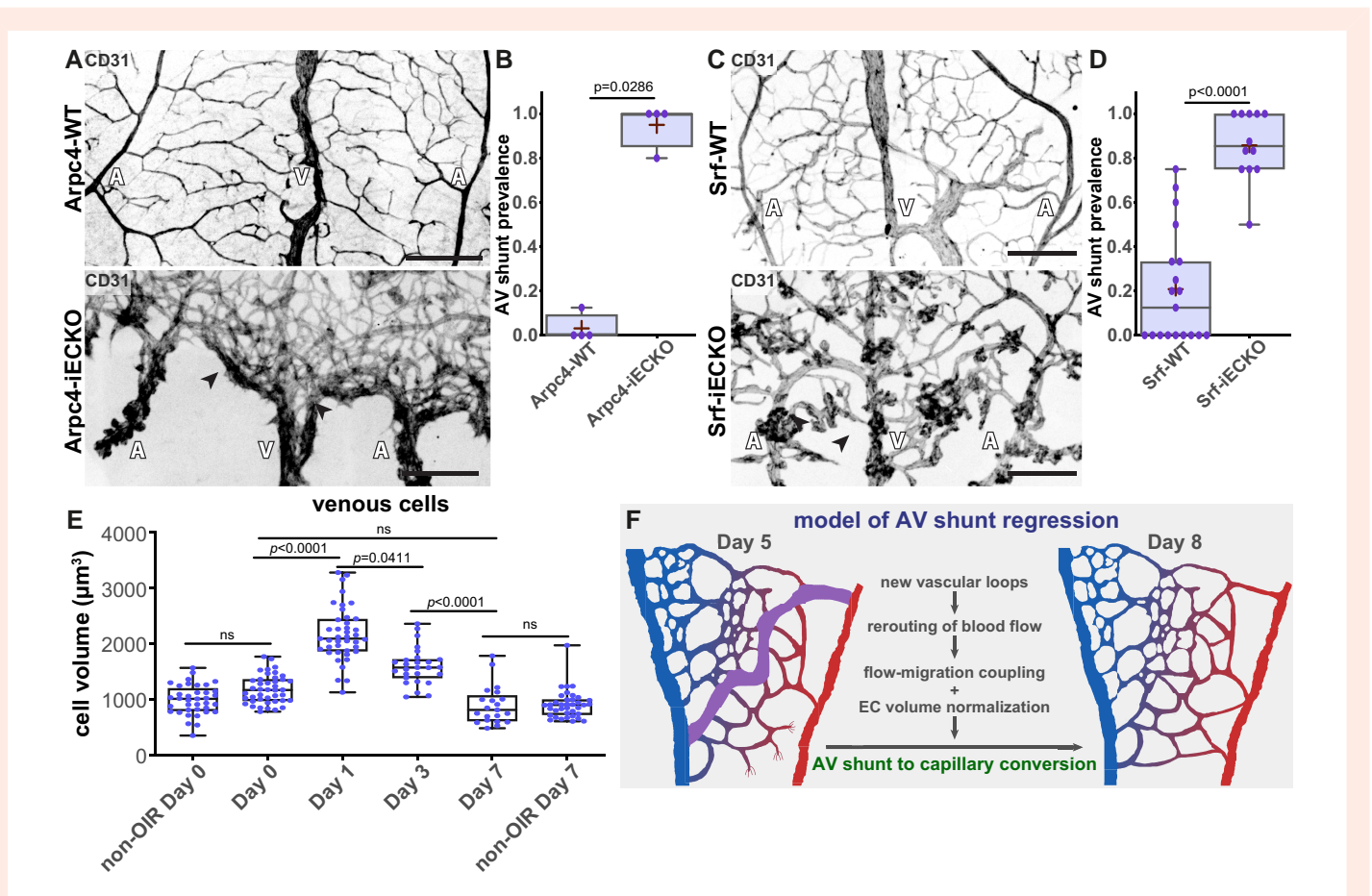
Figure 8 Inhibition of neovascular capillaries prevents AV shunt regression. (A) Representative images of Arpc4-WT (top) and Arpc4-iECKO (bottom) retinas at Day 7 stained for vascular network (CD31, grey). Black arrows: AV shunts; A, artery; V, vein. Scale bar: 200 µm. (B) Quantification of AV shunt prevalence at Day 7 in Arpc4-WT (29 AV sections) and Arpc4-iECKO (16 AV sections) retinas. Each dot represents a mouse retina. *P*-value from Mann–Whitney test. (C) Representative images of Srf-WT (top) and Srf-iECKO (bottom) retinas at Day 9 stained for vascular network (CD31, grey). Black arrows: AV shunts; A, artery; V, vein. Scale bar: 200 µm. (D) Quantification of AV shunt prevalence at Day 9 in Srf-WT (86 AV sections) and Srf-iECKO (63 AV sections) retinas. Each dot represents a mouse retina. *P*-value from Mann–Whitney test. (E) Quantification of venous (vein and venous capillaries) EC volume at Day 0, Day 1, Day 3, and Day 7 and of non-OIR mouse retinas corresponding to time points Day 0 (P11) and Day 7 (P18). Each dot represents one EC from Day 0 (42 cells, 3 pups); Day 1 (41 cells, 3 pups); Day 3 (27 cells, 3 pups); Day 7 (21 cells, 5 pups); non-OIR Day 0 (37 cells, 5 pups); and non-OIR Day 7 (37 cells, 5 pups). *P*-values from Kruskal–Wallis test with Dunn's correction for multiple comparisons. (F) Model describing AV shunt regression in OIR protocol.

Alk1 deficiency together with OIR protocol led to a further increase in venous EC hypertrophy. This may suggest that either Alk1 signalling inhibition may further activate the mTOR pathway in OIR conditions or that Alk1 signalling activates EC hypertrophy via a distinct mechanism. Further studies are required to unravel these questions.

Finally, we found that ALK1 EC-LOF leads to venous EC hypertrophy in angiogenic conditions whilst no changes are observed in quiescent conditions (see Supplementary material online, *Figure S8H*). This is consistent with the fact that BMP LOF mouse models require pro-angiogenic stimuli (inflammation, wounding, or VEGF injection) to promote AVM formation. Thus, we propose that BMP9/10-ALK1 signalling may act as an active mechanism of EC volume control in pro-angiogenic environments.

Despite the strong evidence of cell volume as a key mechanism driving AVM formation, how EC volume-dependent lumen enlargement feedbacks into flow dysregulation that promotes capillary-to-shunt conversion remains largely obscure. Through a rheological perspective, differential resistance of capillary vessel segments would explain preferential shunting of flow through enlarged vessels, yet vascular cells have evolved numerous mechanisms tightly controlling blood flow, with a particular emphasis on mural cells.[81] Thus, it is likely that additional mechanisms related to mural

cell activity may be affected in our model which further promotes AV shunt development. Interestingly, recent reports have also linked mural cell function and AVM formation in animal models.[82–84] Yet, from our perspective, the dysfunction of mural cell-dependent flow control is a facilitator rather than a driver and pre-requires an imbalance in EC volume as an initiating step, as suggested by our modelling analysis.

Finally, our work also establishes a solid model to investigate AVM regression. How and why genetically driven AVMs do not regress is a key open question. Recently, thalidomide treatment has shown promising effects on the regression of AVMs in patients with a severely symptomatic AVM that is refractory to conventional therapies.[85,86] Yet, the molecular mechanisms of the action of this broad-spectrum drug remain unclear. Taking our results into consideration, we can propose that thalidomide may either promote cell volume normalization and/or efficient flow-migration coupling-induced remodelling.

Moreover, our novel insights into AV shunt regression also open the perspective of a novel class of mutations that might be associated with human AVMs. As AV shunts can naturally occur in genetically competent individuals, mutations impacting AV shunt resolution mechanisms, rather than AV shunt formation mechanisms, could promote the stabilization

and growth of those lesions by a lack of capacity to resolve them. Given that mutations in Srf and Arp2/3 complex limit new sprout formation and AV shunt regression, we predict that mutations impacting EC motility and sprouting when associated with naturally occurring shunts may lead to AVMs.

The mouse retina constitutes a very solid model to investigate key mechanisms regulating vascular biology and disease, including AVMs. However, it's important to note that the structural and organizational differences between the mouse retina and human retina, as well as other tissues, are considerable. Therefore, further studies are needed to determine the broader applicability of the mechanisms we have described, both in human contexts and across different organs. In addition, our SRF and ARPC4 mouse models showed a small reduction in the formation of AV shunts. We hypothesized that this is due to reduced cell migration towards the AV shunt, as predicted by the flow-migration coupling model. Yet, we cannot rule out that the decreased sprouting capacity of ECs observed in these animals may contribute to this effect.

In conclusion, we demonstrated that EC volume is the key mechanism driving AVM formation, and it seems transversal to genetic and non-genetic AVM mouse models. Our data strongly underline the necessity to further investigate the mechanisms regulating EC volume in health and disease as a way to identify therapeutic approaches to prevent and revert AVMs.

Supplementary material

Supplementary material is available at *Cardiovascular Research* online.

Authors' contributions

Conceptualization: M.O., A.P., D.R., R.E., M.O.B., S.P.O., C.A.F. Methodology: M.O., A.P., D.R., N.V.C., T.C., S.P.O., C.A.F. Experimentation and data acquisition: M.O., A.P., D.R., N.V.C., T.C., A.M.F., M.P.S., Y.C., L.H.M., C.A.F. Data analysis: M.O., A.P., D.R, N.V.C., T.C., R.E., M.O.B., C.A.F. Project administration: C.A.F.. Writing—original draft: M.O., C.A.F. Writing—review and editing: M.O., A.P., D.R., N.V.C., L.H.M., S.P.O., C.A.F.

Data availability

The data underlying this article will be shared on reasonable request to the corresponding author.

References

1. Alaraj A, Shakur SF, Amin-Hanjani S, Mostafa H, Khan S, Aletich VA, Charbel FT. Changes in wall shear stress of cerebral arteriovenous malformation feeder arteries after embolization and surgery. *Stroke* 2015;**46**:1216–1220.
2. Steiger HJ. Recent progress understanding pathophysiology and genesis of brain AVM-a narrative review. *Neurosurg Rev* 2021;**44**:3165–3175.
3. Couto JA, Huang AY, Konczyk DJ, Goss JA, Fishman SJ, Mulliken JB, Warman ML, Greene AK. Somatic MAP2K1 mutations are associated with extracranial arteriovenous malformation. *Am J Hum Genet* 2017;**100**:546–554.
4. Nikolaev SI, Vetiska S, Bonilla X, Boudreau E, Jauhiainen S, Rezai Jahromi B, Khyzha N, DiStefano PV, Suutarinen S, Kiehl TR, Mendes Pereira V, Herman AM, Krings T, Andrade-Barazarte H, Tung T, Valiante T, Zadeh G, Tymianski M, Rauramaa T, Ylä-Herttuala S, Wythe JD, Antonarakis SE, Frösen J, Fish JE, Radovanovic I. Somatic activating KRAS mutations in arteriovenous malformations of the brain. *N Engl J Med* 2018;**378**:250–261.
5. Dupuis-Girod S, Bailly S, Plauchu H. Hereditary hemorrhagic telangiectasia: from molecular biology to patient care. *J Thromb Haemost* 2010;**8**:1447–1456.
6. Robert F, Desroches-Castan A, Bailly S, Dupuis-Girod S, Feige JJ. Future treatments for hereditary haemorrhagic telangiectasia. *Orphanet J Rare Dis* 2020;**15**:4.
7. Johnson DW, Berg JN, Baldwin MA, Gallione CJ, Marondel I, Yoon SJ, Stenzel TT, Speer M, Pericak-Vance MA, Diamond A, Guttmacher AE, Jackson CE, Attisano L, Kucherlapati R, Porteous ME, Marchuk DA. Mutations in the activin receptor-like kinase 1 gene in hereditary haemorrhagic telangiectasia type 2. *Nat Genet* 1996;**13**:189–195.
8. Lesca G, Burnichon N, Raux G, Tosi M, Pinson S, Marion MJ, Babin E, Gilbert-Dussardier B, Rivière S, Goizet C, Faivre L, Plauchu H, Frébourg T, Calender A, Giraud S; French Rendu-Osler Network. Distribution of ENG and ACVRL1 (ALK1) mutations in French HHT patients. *Hum Mutat* 2006;**27**:598.
9. McAllister KA, Grogg KM, Johnson DW, Gallione CJ, Baldwin MA, Jackson CE, Helmbold EA, Markel DS, McKinnon WC, Murrell J, McCormick MK, Pericak-Vance MA, Heutink P, Oostra BA, Haitjema T, Westerman CJJ, Porteous ME, Guttmacher AE, Letarte M, Marchuk DA. Endoglin, a TGF-beta binding protein of endothelial cells, is the gene for hereditary haemorrhagic telangiectasia type 1. *Nat Genet* 1994;**8**:345–351.
10. Gallione CJ, Repetto GM, Legius E, Rustgi AK, Schelley SL, Tejpar S, Mitchell G, Drouin E, Westermann CJ, Marchuk DA. A combined syndrome of juvenile polyposis and hereditary haemorrhagic telangiectasia associated with mutations in MADH4 (SMAD4). *Lancet* 2004;**363**:852–859.
11. Gallione CJ, Richards JA, Letteboer TG, Rushlow D, Prigoda NL, Leedom TP, Ganguly A, Castells A, Ploos van Amstel JK, Westermann CJ, Pyeritz RE, Marchuk DA. SMAD4 mutations found in unselected HHT patients. *J Med Genet* 2006;**43**:793–797.
12. Hernandez F, Huether R, Carter L, Johnston T, Thompson J, Gossage JR, Chao E, Elliott AM. Mutations in RASA1 and GDF2 identified in patients with clinical features of hereditary hemorrhagic telangiectasia. *Hum Genome Var* 2015;**2**:15040.
13. Liu J, Yang J, Tang X, Li H, Shen Y, Gu W, Zhao S. Homozygous GDF2-related hereditary hemorrhagic telangiectasia in a Chinese family. *Pediatrics* 2020;**146**:e20191970.
14. Topiwala KK, Patel SD, Nouh AM, Alberts MJ. Novel GDF2 gene mutation associated with pulmonary arteriovenous malformation. *J Stroke Cerebrovasc Dis* 2020;**29**:105301.
15. Wooderchak-Donahue WL, McDonald J, O'Fallon B, Upton PD, Li W, Roman BL, Young S, Plant P, Fülöp GT, Langa C, Morrell NW, Botella LM, Bernabeu C, Stevenson DA, Runo JR, Bayrak-Toydemir P. BMP9 mutations cause a vascular-anomaly syndrome with phenotypic overlap with hereditary hemorrhagic telangiectasia. *Am J Hum Genet* 2013;**93**:530–537.
16. Lee HW, Xu Y, He L, Choi W, Gonzalez D, Jin S-W, Simons M. Role of venous endothelial cells in developmental and pathologic angiogenesis. *Circulation* 2021;**144**:1308–1322.
17. Park H, Furtado J, Poulet M, Chung M, Yun S, Lee S, Sessa WC, Franco CA, Schwartz MA, Eichmann A. Defective flow-migration coupling causes arteriovenous malformations in hereditary hemorrhagic telangiectasia. *Circulation* 2021;**144**:805–822.
18. Singh E, Redgrave RE, Phillips HM, Arthur HM. Arterial endoglin does not protect against arteriovenous malformations. *Angiogenesis* 2020;**23**:559–566.
19. Baeyens N, Larrivee B, Ola R, Hayward-Piatkowskyi B, Dubrac A, Huang B, Ross TD, Coon BG, Min E, Tsarfati M, Tong H, Eichmann A, Schwartz MA. Defective fluid shear stress mechanotransduction mediates hereditary hemorrhagic telangiectasia. *J Cell Biol* 2016;**214**:807–816.
20. Corti P, Young S, Chen CY, Patrick MJ, Rochon ER, Pekkan K, Roman BL. Interaction between alk1 and blood flow in the development of arteriovenous malformations. *Development* 2011;**138**:1573–1582.
21. Jin Y, Muhl L, Burmakin M, Wang Y, Duchez AC, Betsholtz C, Arthur HM, Jakobsson L. Endoglin prevents vascular malformation by regulating flow-induced cell migration and specification through VEGFR2 signalling. *Nat Cell Biol* 2017;**19**:639–652.
22. Murphy PA, Kim TN, Lu G, Bollen AW, Schaffer CB, Wang RA. Notch4 normalization reduces blood vessel size in arteriovenous malformations. *Sci Transl Med* 2012;**4**:117ra8.
23. Park SO, Lee YJ, Seki T, Hong KH, Fliess N, Jiang Z, Park A, Wu X, Kaartinen V, Roman BL, Oh SP. ALK5- and TGFBR2-independent role of ALK1 in the pathogenesis of hereditary hemorrhagic telangiectasia type 2. *Blood* 2008;**111**:633–642.
24. Park SO, Wankhede M, Lee YJ, Choi EJ, Fliess N, Choe SW, Oh SH, Walter G, Raizada MK, Sorg BS, Oh SP. Real-time imaging of de novo arteriovenous malformation in a mouse model of hereditary hemorrhagic telangiectasia. *J Clin Invest* 2009;**119**:3487–3496.
25. Ola R, Dubrac A, Han J, Zhang F, Fang JS, Larrivee B, Lee M, Urarte AA, Kraehling JR, Genet G, Hirschi KK, Sessa WC, Canals FV, Graupera M, Yan M, Young LH, Oh PS, Eichmann A. PI3 kinase inhibition improves vascular malformations in mouse models of hereditary haemorrhagic telangiectasia. *Nat Commun* 2016;**7**:13650.
26. Han C, Choe SW, Kim YH, Acharya AP, Keselowsky BG, Sorg BS, Lee YJ, Oh SP. VEGF neutralization can prevent and normalize arteriovenous malformations in an animal model for hereditary hemorrhagic telangiectasia 2. *Angiogenesis* 2014;**17**:823–830.
27. Ruiz S, Zhao H, Chandakkar P, Papoin J, Choi H, Nomura-Kitabayashi A, Patel R, Gillen M, Diao L, Chatterjee PK, He M, Al-Abed Y, Wang P, Metz CN, Oh SP, Blanc L, Campagne F,

Marambaud P. Correcting Smad1/5/8, mTOR, and VEGFR2 treats pathology in hereditary hemorrhagic telangiectasia models. *J Clin Invest* 2020;**130**:942–957.

28. Fish JE, Flores Suarez CP, Boudreau E, Herman AM, Gutierrez MC, Gustafson D, DiStefano PV, Cui M, Chen Z, De Ruiz KB, Schexnayder TS, Ward CS, Radovanovic I, Wythe JD. Somatic gain of KRAS function in the endothelium is sufficient to cause vascular malformations that require MEK but not PI3K signaling. *Circ Res* 2020;**127**:727–743.

29. Crist AM, Lee AR, Patel NR, Westhoff DE, Meadows SM. Vascular deficiency of Smad4 causes arteriovenous malformations: a mouse model of Hereditary Hemorrhagic Telangiectasia. *Angiogenesis* 2018;**21**:363–380.

30. Sugden WW, Meissner S, Aegerter-Wilmsen T, Tsaryk R, Leonard EV, Bussmann J, Hamm MJ, Herzog W, Jin Y, Jakobsson L, Denz C, Siekmann AF. Endoglin controls blood vessel diameter through endothelial cell shape changes in response to haemodynamic cues. *Nat Cell Biol* 2017;**19**:653–665.

31. Rochon ER, Menon PG, Roman BL. Alk1 controls arterial endothelial cell migration in lumenized vessels. *Development* 2016;**143**:2593–2602.

32. Banerjee K, Lin Y, Gahn J, Cordero J, Gupta P, Mohamed I, Graupera M, Dobreva G, Schwartz MA, Ola R. SMAD4 maintains the fluid shear stress set point to protect against arterial-venous malformations. *J Clin Invest* 2023;**133**:e168352. doi:10.1172/JCI168352.

33. Barbacena P, Ouarne M, Haigh JJ, Vasconcelos FF, Pezzarossa A, Franco CA. GNrep mouse: a reporter mouse for front-rear cell polarity. *Genesis* 2019;**57**:e23299.

34. Krndija D, El Marjou F, Guirao B, Richon S, Leroy O, Bellaiche Y, Hannezo E, Matic Vignjevic D. Active cell migration is critical for steady-state epithelial turnover in the gut. *Science* 2019;**365**:705–710.

35. Parlakian A, Tuil D, Hamard G, Tavernier G, Hentzen D, Concordet JP, Paulin D, Li Z, Daegelen D. Targeted inactivation of serum response factor in the developing heart results in myocardial defects and embryonic lethality. *Mol Cell Biol* 2004;**24**:5281–5289.

36. Muzumdar MD, Tasic B, Miyamichi K, Li L, Luo L. A global double-fluorescent Cre reporter mouse. *Genesis* 2007;**45**:593–605.

37. Sorensen I, Adams RH, Gossler A. DLL1-mediated Notch activation regulates endothelial identity in mouse fetal arteries. *Blood* 2009;**113**:5680–5688.

38. Claxton S, Kostourou V, Jadeja S, Chambon P, Hodivala-Dilke K, Fruttiger M. Efficient, inducible Cre-recombinase activation in vascular endothelium. *Genesis* 2008;**46**:74–80.

39. Bernabeu MO, Jones ML, Nash RW, Pezzarossa A, Coveney PV, Gerhardt H, Franco CA. PolNet: a tool to quantify network-level cell polarity and blood flow in vascular remodeling. *Biophys J* 2018;**114**:2052–2058.

40. Carvalho JR, Fortunato IC, Fonseca CG, Pezzarossa A, Barbacena P, Dominguez-Cejudo MA, Vasconcelos FF, Santos NC, Carvalho FA, Franco CA. Non-canonical Wnt signaling regulates junctional mechanocoupling during angiogenic collective cell migration. *Elife* 2019;**8**:e45853.

41. Schindelin J, Arganda-Carreras I, Frise E, Kaynig V, Longair M, Pietzsch T, Preibisch S, Rueden C, Saalfeld S, Schmid B, Tinevez J-Y, White DJ, Hartenstein V, Eliceiri K, Tomancak P, Cardona A. Fiji: an open-source platform for biological-image analysis. *Nat Methods* 2012;**9**:676–682.

42. McDowell KP, Berthiaume AA, Tieu T, Hartmann DA, Shih AY. VasoMetrics: unbiased spatiotemporal analysis of microvascular diameter in multi-photon imaging applications. *Quant Imaging Med Surg* 2021;**11**:969–982.

43. Pries AR, Secomb TW. Microvascular blood viscosity in vivo and the endothelial surface layer. *Am J Physiol Heart Circ Physiol* 2005;**289**:H2657–H2664.

44. Pries AR, Secomb TW, Gaehtgens P, Gross JF. Blood flow in microvascular networks. Experiments and simulation. *Circ Res* 1990;**67**:826–834.

45. Bernabeu MO, Jones ML, Nielsen JH, Krüger T, Nash RW, Groen D, Schmieschek S, Hetherington J, Gerhardt H, Franco CA, Coveney PV. Computer simulations reveal complex distribution of haemodynamic forces in a mouse retina model of angiogenesis. *J R Soc Interface* 2014;**11**:20140543.

46. Ricci B. Oxygen-induced retinopathy in the rat model. *Doc Ophthalmol* 1990;**74**:171–177.

47. Scott A, Fruttiger M. Oxygen-induced retinopathy: a model for vascular pathology in the retina. *Eye (Lond)* 2010;**24**:416–421.

48. Penn JS, Madan A, Caldwell RB, Bartoli M, Caldwell RW, Hartnett ME. Vascular endothelial growth factor in eye disease. *Prog Retin Eye Res* 2008;**27**:331–371.

49. Chang E, Nayak L, Jain MK. Kruppel-like factors in endothelial cell biology. *Curr Opin Hematol* 2017;**24**:224–229.

50. Ola R, Kunzel SH, Zhang F, Genet G, Chakraborty R, Pibouin-Fragner L, Martin K, Sessa W, Dubrac A, Eichmann A. SMAD4 prevents flow induced arteriovenous malformations by inhibiting casein kinase 2. *Circulation* 2018;**138**:2379–2394.

51. Luo W, Garcia-Gonzalez I, Fernandez-Chacon M, Casquero-Garcia V, Sanchez-Munoz MS, Muhleder S, Garcia-Ortega L, Andrade J, Potente M, Benedito R. Arterialization requires the timely suppression of cell growth. *Nature* 2021;**589**:437–441.

52. Murphy PA, Kim TN, Huang L, Nielsen CM, Lawton MT, Adams RH, Schaffer CB, Wang RA. Constitutively active Notch4 receptor elicits brain arteriovenous malformations through enlargement of capillary-like vessels. *Proc Natl Acad Sci U S A* 2014;**111**:18007–18012.

53. Verweij J, Pinedo HM. Mitomycin C: mechanism of action, usefulness and limitations. *Anticancer Drugs* 1990;**1**:5–13.

54. Figueiredo AM, Barbacena P, Russo A, Vaccaro S, Ramalho D, Pena A, Lima AP, Ferreira RR, Fidalgo MA, El-Marjou F, Carvalho Y, Vasconcelos FF, Lennon-Dumenil AM, Vignjevic DM, Franco CA. Endothelial cell invasion is controlled by dactylopodia. *Proc Natl Acad Sci U S A* 2021;**118**:e2023829118.

55. Franco CA, Blanc J, Parlakian A, Blanco R, Aspalter IM, Kazakova N, Diguet N, Mylonas E, Gao-Li J, Vaahtokari A, Penard-Lacronique V, Fruttiger M, Rosewell I, Mericskay M, Gerhardt H, Li Z. SRF selectively controls tip cell invasive behavior in angiogenesis. *Development* 2013;**140**:2321–2333.

56. Franco CA, Mericskay M, Parlakian A, Gary-Bobo G, Gao-Li J, Paulin D, Gustafsson E, Li Z. Serum response factor is required for sprouting angiogenesis and vascular integrity. *Dev Cell* 2008;**15**:448–461.

57. Weinl C, Riehle H, Park D, Stritt C, Beck S, Huber G, Wolburg H, Olson EN, Seeliger MW, Adams RH, Nordheim A. Endothelial SRF/MRTF ablation causes vascular disease phenotypes in murine retina. *J Clin Invest* 2013;**123**:2193–2206.

58. Aspalter IM, Gordon E, Dubrac A, Ragab A, Narloch J, Vizan P, Geudens I, Collins RT, Franco CA, Abrahams CL, Thurston G, Fruttiger M, Rosewell I, Eichmann A, Gerhardt H. Alk1 and Alk5 inhibition by Nrp1 controls vascular sprouting downstream of Notch. *Nat Commun* 2015;**6**:7264.

59. Hikita T, Mirzapourshafiyi F, Barbacena P, Riddell M, Pasha A, Li M, Kawamura T, Brandes RP, Hirose T, Ohno S, Gerhardt H, Matsuda M, Franco CA, Nakayama M. PAR-3 controls endothelial planar polarity and vascular inflammation under laminar flow. *EMBO Rep* 2018;**19**:e45253.

60. Rohlenova K, Veys K, Miranda-Santos I, De Bock K, Carmeliet P. Endothelial cell metabolism in health and disease. *Trends Cell Biol* 2018;**28**:224–236.

61. Pajak B, Siwiak E, Soltyka M, Priebe A, Zielinski R, Fokt I, Ziemniak M, Jaskiewicz A, Borowski R, Domoradzki T, Priebe W. 2-Deoxy-d-glucose and its analogs: from diagnostic to therapeutic agents. *Int J Mol Sci* 2019;**21**:234.

62. De Bock K, Georgiadou M, Schoors S, Kuchnio A, Wong BW, Cantelmo AR, Quaegebeur A, Ghesquiere B, Cauwenberghs S, Eelen G, Phng LK, Betz I, Tembuyser B, Brepoels K, Welti J, Geudens I, Segura I, Cruys B, Bifari F, Decimo I, Blanco R, Wyns S, Vangindertael J, Rocha S, Collins RT, Munck S, Daelemans D, Imamura H, Devlieger R, Rider M, Van Veldhoven PP, Schuit F, Bartrons R, Hofkens J, Fraisl P, Telang S, Deberardinis RJ, Schoonjans L, Vinckier S, Chesney J, Gerhardt H, Dewerchin M, Carmeliet P. Role of PFKFB3-driven glycolysis in vessel sprouting. *Cell* 2013;**154**:651–663.

63. Saxton RA, Sabatini DM. mTOR signaling in growth, metabolism, and disease. *Cell* 2017;**168**:960–976.

64. Tual-Chalot S, Mahmoud M, Allinson KR, Redgrave RE, Zhai Z, Oh SP, Fruttiger M, Arthur HM. Endothelial depletion of Acvrl1 in mice leads to arteriovenous malformations associated with reduced endoglin expression. *PLoS One* 2014;**9**:e98646.

65. Barbacena P, Dominguez-Cejudo M, Fonseca CG, Gomez-Gonzalez M, Faure LM, Zarkada G, Pena A, Pezzarossa A, Ramalho D, Giarratano Y, Ouarne M, Barata D, Fortunato IC, Misikova LH, Mauldin I, Carvalho Y, Trepat X, Roca-Cusachs P, Eichmann A, Bernabeu MO, Franco CA. Competition for endothelial cell polarity drives vascular morphogenesis in the mouse retina. *Dev Cell* 2022;**57**:2321–2333.e9.

66. Franco CA, Jones ML, Bernabeu MO, Geudens I, Mathivet T, Rosa A, Lopes FM, Lima AP, Ragab A, Collins RT, Phng LK, Coveney PV, Gerhardt H. Dynamic endothelial cell rearrangements drive developmental vessel regression. *PLoS Biol* 2015;**13**:e1002125.

67. Franco CA, Jones ML, Bernabeu MO, Vion A-C, Barbacena P, Fan J, Mathivet T, Fonseca CG, Ragab A, Yamaguchi TP, Coveney PV, Lang RA, Gerhardt H. Non-canonical Wnt signalling modulates the endothelial shear stress flow sensor in vascular remodelling. *Elife* 2016;**5**:e07727.

68. Ouarne M, Pena A, Franco CA. From remodeling to quiescence: the transformation of the vascular network. *Cells Dev* 2021;**168**:203735.

69. Nielsen CM, Zhang X, Raygor K, Wang S, Bollen AW, Wang RA. Endothelial Rbpj deletion normalizes Notch4-induced brain arteriovenous malformation in mice. *J Exp Med* 2023;**220**:e20211390.

70. Cadart C, Venkova L, Recho P, Lagomarsino MC, Piel M. The physics of cell-size regulation across timescales. *Nat Phys* 2019;**15**:993–1004.

71. Sachs F, Sivaselvan MV. Cell volume control in three dimensions: water movement without solute movement. *J Gen Physiol* 2015;**145**:373–380.

72. Schmelzle T, Hall MN. TOR, a central controller of cell growth. *Cell* 2000;**103**:253–262.

73. Dang CV. MYC, metabolism, cell growth, and tumorigenesis. *Cold Spring Harb Perspect Med* 2013;**3**:a014217.

74. Schuhmacher M, Staege MS, Pajic A, Polack A, Weidle UH, Bornkamm GW, Eick D, Kohlhuber F. Control of cell growth by c-Myc in the absence of cell division. *Curr Biol* 1999;**9**:1255–1258.

75. Dong J, Feldmann G, Huang J, Wu S, Zhang N, Comerford SA, Gayyed MF, Anders RA, Maitra A, Pan D. Elucidation of a universal size-control mechanism in Drosophila and mammals. *Cell* 2007;**130**:1120–1133.

76. Mugahid D, Kalocsay M, Liu X, Gruver JS, Peshkin L, Kirschner MW. YAP regulates cell size and growth dynamics via non-cell autonomous mediators. *Elife* 2020;**9**:e53404.

77. Yu FX, Zhao B, Guan KL. Hippo pathway in organ size control, tissue homeostasis, and cancer. *Cell* 2015;**163**:811–828.

78. Guo M, Pegoraro AF, Mao A, Zhou EH, Arany PR, Han Y, Burnette DT, Jensen MH, Kasza KE, Moore JR, Mackintosh FC, Fredberg JJ, Mooney DJ, Lippincott-Schwartz J, Weitz DA. Cell volume change through water efflux impacts cell stiffness and stem cell fate. *Proc Natl Acad Sci U S A* 2017;**114**:E8618–E8627.

79. Perez Gonzalez N, Tao J, Rochman ND, Vig D, Chiu E, Wirtz D, Sun SX. Cell tension and mechanical regulation of cell volume. *Mol Biol Cell* 2018;**29**:0.

80. Zhu W, Saw D, Weiss M, Sun Z, Wei M, Shaligram S, Wang S, Su H. Induction of brain arteriovenous malformation through CRISPR/Cas9-mediated somatic Alk1 gene mutations in adult mice. *Transl Stroke Res* 2019;**10**:557–565.

81. Longden TA, Zhao G, Hariharan A, Lederer WJ. Pericytes and the control of blood flow in brain and heart. *Annu Rev Physiol* 2023;**85**:137–164.

82. Li F, Lan Y, Wang Y, Wang J, Yang G, Meng F, Han H, Meng A, Wang Y, Yang X. Endothelial Smad4 maintains cerebrovascular integrity by activating N-cadherin through cooperation with Notch. *Dev Cell* 2011;**20**:291–302.

83. Nadeem T, Bogue W, Bigit B, Cuervo H. Deficiency of Notch signaling in pericytes results in arteriovenous malformations. *JCI Insight* 2020;**5**:e125940.

84. Pan P, Shaligram SS, Do Prado LB, He L, Su H. The role of mural cells in hemorrhage of brain arteriovenous malformation. *Brain Hemorrhages* 2021;**2**:49–56.

85. Boon LM, Dekeuleneer V, Coulie J, Marot L, Bataille A-C, Hammer F, Clapuyt P, Jeanjean A, Dompmartin A, Vikkula M. Case report study of thalidomide therapy in 18 patients with severe arteriovenous malformations. *Nat Cardiovasc Res* 2022;**1**: 562–567.

86. Lebrin F, Srun S, Raymond K, Martin S, van den Brink S, Freitas C, Breant C, Mathivet T, Larrivee B, Thomas JL, Arthur HM, Westermann CJ, Disch F, Mager JJ, Snijder RJ, Eichmann A, Mummery CL. Thalidomide stimulates vessel maturation and reduces epistaxis in individuals with hereditary hemorrhagic telangiectasia. *Nat Med* 2010;**16**: 420–428.